

---

This is a partially peer-reviewed preprint submitted to EarthArXiv.  
This revised manuscript has been submitted to *Environmental Science and Technology* to be reviewed for  
publication.  
Later versions of this manuscript may have different content.  
The authors welcome feedback.

---

# Extension of Methane Emission Rate Distribution for Permian Basin Oil and Gas Production Infrastructure by Aerial LiDAR

<sup>1</sup> William M. Kunkel,\* Asa E. Carre-Burritt, Grant S. Aivazian, Nicholas C. Snow,  
Jacob T. Harris, Tagert S. Mueller, Peter A. Roos, and Michael J. Thorpe\*  
*Bridger Photonics, Inc., 2310 University Way Bldg 4-4, Bozeman, MT 59715, USA*

E-mail: William.Kunkel@bridgerphotonics.com; Mike.Thorpe@bridgerphotonics.com

## Abstract

<sup>2</sup>  
<sup>3</sup> Aerial LiDAR measurements at 7474 oil and gas production facilities in the Per-  
<sup>4</sup> mian Basin yield a measured methane emission rate distribution extending to the de-  
<sup>5</sup> tection sensitivity of the method, 2 kg/h at 90% probability of detection. Emissions are  
<sup>6</sup> found at 38.3% of facilities scanned, a significantly higher proportion than reported in  
<sup>7</sup> lower-sensitivity campaigns. LiDAR measurements are analyzed in combination with  
<sup>8</sup> measurements of the heavy tail portion of the distribution ( $> 600$  kg/h) obtained from  
<sup>9</sup> an airborne solar infrared imaging spectrometry campaign by Carbon Mapper (CM).  
<sup>10</sup> A joint distribution is found by fitting the aligned LiDAR and CM data. By comparing  
<sup>11</sup> the aerial samples to the joint distribution, the practical detection sensitivity of the CM  
<sup>12</sup> 2019 campaign is found to be 280 kg/h [256, 309] (95% confidence) at 50% probability  
<sup>13</sup> of detection for facility-sized emission sources. With respect to the joint distribution,  
<sup>14</sup> the LiDAR campaign is found to have measured 103.6% [93.5%, 114.2%] of the total  
<sup>15</sup> emission rate from equipment-sized emission sources ( $\sim 2$  m diameter) with emission  
<sup>16</sup> rates above 3 kg/h, whereas the CM 2019 campaign is found to have measured 39.7%

17 [34.6%, 45.1%] of the same quantity for facility-sized sources (150 m diameter) above  
18 10 kg/h. The analysis is repeated with data from CM 2020-21 campaigns, with sim-  
19 ilar results. The combined distributions represent a more comprehensive view of the  
20 emission rate distribution in the survey area, revealing the significance of previously un-  
21 derreported emission sources at rates below the detection sensitivity of some emissions  
22 monitoring campaigns.

## 23 **Synopsis**

24 New methane emission measurements in the Permian Basin extend the distribution of source  
25 emission rates beyond the sensitivity limits of previous studies by two orders of magnitude.

## 26 **Introduction**

27 Methane is a potent greenhouse gas with a warming potential 80 times greater than that of  
28 CO<sub>2</sub> in a 20-year time frame.<sup>1</sup> Its current global emission rate is great enough to impact the  
29 climate significantly, with a greater contribution to global temperature rise in the first ten  
30 years after emission than CO<sub>2</sub> at its respective current emission rate.<sup>2</sup> Consequently, miti-  
31 gation of methane emissions is viewed as particularly important for meeting climate goals  
32 within the next decade. Economic sectors including agriculture, waste disposal, and energy  
33 are recognized as leading contributors to anthropogenic methane emissions, representing do-  
34 mains where emissions can be most meaningfully mitigated. In the oil and natural gas (O&G)  
35 industry, emissions arise from discrete infrastructure elements and associated processes that  
36 can often be addressed with targeted intervention. Mitigation involves both the detection of  
37 emission sources and follow-up with repair and/or upgrade of emitting equipment. Identi-  
38 fying the most important emissions drivers and tracking the efficacy of mitigation efforts is  
39 key to making emissions reductions effective and efficient.<sup>3,4</sup>

40 Broadening the view of emissions from individual sources to a distribution of sources

41 provides large-scale context to set meaningful mitigation goals. Past characterization of  
42 methane emission distributions has often relied on bottom-up estimates based on emission  
43 factors, such as those used for the U.S. Environmental Protection Agency’s Greenhouse  
44 Gas Reporting Program and Greenhouse Gas Inventory. These estimates aim to identify  
45 dominant emission sources at the component or equipment levels but have been shown to  
46 misrepresent large-scale methane emissions distributions and the relative contribution of  
47 different elements,<sup>3,5-8</sup> with the greatest discrepancies existing in the production sector.<sup>9</sup>  
48 In addition, emissions factors are meant to apply nationally, whereas emission intensities  
49 in fact vary regionally and mitigation is performed locally.<sup>7,8</sup> To more precisely account for  
50 emissions and to inform mitigation efforts, measurement campaigns have been conducted to  
51 obtain locally relevant empirical data within individual production basins throughout the  
52 United States and Canada.<sup>10-15</sup>

53 Many recent research efforts have focused on the Permian Basin because of its sizable  
54 share of U.S. O&G production, comprising 43% of domestic oil and 22% of natural gas  
55 produced annually.<sup>16</sup> Two studies on 2018/2019 Permian methane emissions both estimated  
56 region-wide O&G methane intensity to be 3.7% of production,<sup>17,18</sup> exceeding an estimated  
57 national average of 2.3% for the full supply chain.<sup>7</sup> More recent work provided methane  
58 intensity estimates in the range of 5-6% in 2018, decreasing to 3-4% in 2020.<sup>19</sup> Aerial mea-  
59 surements conducted in 2019-21 coupled with simulated emission sources representing the  
60 unmeasured part of the distribution provided a Permian Basin methane intensity estimate  
61 of 5.29%.<sup>20</sup> With the exception of Ref. 20, these studies leveraged satellite observations for  
62 inversion modeling and mass balance calculations, which are useful in benchmarking overall  
63 emissions but lack the detection sensitivity or spatial resolution needed to identify individual  
64 methane sources and understand their relation to infrastructure elements.

65 To provide a more specific account of emission sources, Carbon Mapper (CM) and Chen  
66 et al. each reported on measurement campaigns in the Permian Basin using aurally deployed  
67 solar infrared imaging spectrometers. The first CM campaign<sup>21</sup> took place in 2019 and cov-

68 ered 55,000 km<sup>2</sup> in the Midland and Delaware sub-basins located in Texas and New Mexico.  
69 Emission sources were localized and attributed to individual facilities. Repeated sampling of  
70 the same sources was used to evaluate emission intermittency. Highly intermittent sources  
71 (0-25% observed persistence of facility-sized sources) were responsible for 48% of all point  
72 source emissions in the sample. Further campaigns in were run in the Permian Basin in  
73 2020-21<sup>22</sup> in a spatial domain partially overlapping with the 2019 campaign, with otherwise  
74 similar collection parameters.

75 The study by Chen et al.<sup>23</sup> was focused on the New Mexico Permian and encompassed  
76 over 90% of wellheads in that region. Chen compared the measured emission rate distribution  
77 from their study to CM 2019 in an overlapping spatial region and found that the CM 2019  
78 campaign detected progressively fewer emission sources at rates below roughly 300 kg/h,  
79 while their own study observed similarly reduced detections below 100-150 kg/h. Though  
80 the decline in detected emission sources suggests that the CM 2019 data underrepresent the  
81 actual emission sources present below the detection sensitivity, the heavy tail portion of the  
82 data set can still valuably inform models of the emission rate distribution.

83 For the present work, CM data are combined and compared to compiled survey data from  
84 Bridger Photonics' first generation Gas Mapping LiDAR (GML) sensor. Emission rates in  
85 the range of 3-300 kg/h, which are underrepresented in the CM campaigns, are detected  
86 by GML at their true frequency. In a complementary manner, the CM campaign data sets  
87 offer extensive sampling of large-rate but infrequently-emitting sources. Detection data from  
88 CM and GML campaigns are joined to obtain a comprehensive view of the emission rate  
89 distribution in the survey region. Emission sources at rates observable by GML but not by  
90 CM are seen to contribute most of the total rate for the whole distribution.

## 91 Methods

92 The Bridger Photonics Gas Mapping LiDAR<sup>TM</sup> (GML) instrument is an aircraft-mounted  
93 remote sensing device that maps methane concentration with coaligned dual LiDAR mea-  
94 surements, GNSS, and aerial photography to show plume shape, identify the source of the  
95 emission, and quantify the emission rate. Coaligned range-finding and gas absorption lasers  
96 are spatially scanned in a conical pattern below the aircraft. Return signal originating  
97 from ground-based backscatter is detected at the sensor. Path-integrated gas concentration  
98 is measured using wavelength modulation spectroscopy on the 1651 nm absorption line of  
99 methane. Flux rates are found from total methane concentration integrated along the di-  
100 rection perpendicular to the gas flow direction, multiplied by wind speed at the measured  
101 plume height. Details of the collection platform have been described previously.<sup>24</sup>

102 For the surveys used in this paper, the GML instrument was flown at a flight altitude  
103 of 206 m, with a measured detection sensitivity of 0.41 kg/h per m/s wind speed at 90%  
104 probability of detection,<sup>25</sup> or 2 kg/h at the average wind speed of 4.9 m/s in Midland, TX.<sup>26</sup>  
105 Scan parameters are chosen so the distance between LiDAR measurement points on the  
106 ground is at maximum 1 m.

107 The CM campaigns in this paper utilize two similar instruments called GAO and AVIRIS-  
108 NG based on solar infrared spectroscopic imaging. The CM data offer extensive sampling of  
109 the heavy tail of the distribution, but lower detection sensitivity and reduced spatial source  
110 resolution compared to GML. The instruments were flown at flight altitudes of 4.5 km and  
111 8 km.<sup>21</sup> High flight altitudes like these offer greater coverage rates (land area per time), but  
112 lower detection sensitivity. Performance of the CM instrument as a function of altitude has  
113 been characterized in controlled releases<sup>27</sup> and modeled with a robust Bayesian approach.<sup>28</sup>

114 Whereas the spatial pixel size increases with altitude (CM: 3-8 m for 3-8 km flight alti-  
115 tude<sup>29,30</sup>), it is important to distinguish between pixel size and source resolution, or spatial  
116 area over which detected emissions are considered to come from the same source. An emis-  
117 sion “source” in this paper means a set of synchronously or asynchronously detected plumes

118 falling into a defined aggregation area, whereas “emitter” means a source smaller than the  
119 source resolution of the measurement system, inclusive of processing. In addition to limits  
120 imposed by image resolution, CM employs a 150 m diameter aggregation area to define its  
121 sources at roughly the size of a typical well pad.

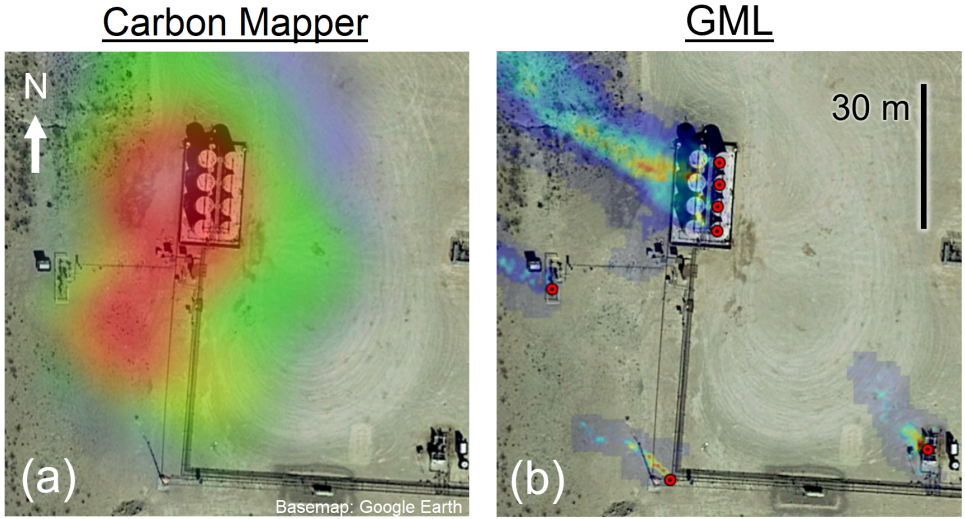


Figure 1: Example facility overlay with methane plume images from (a) CM 2019<sup>31</sup> and (b) GML scans superimposed on satellite imagery. GML emission locations are marked by red dots. CM 2019 and GML plumes were observed on different dates; the GML image comprises plumes observed on multiple dates. GML identifies unique emission sources at an interval of 4-5 m on a tank battery (upper center).

122 To compare spatial characteristics of GML and CM emission sources, consider the exam-  
123 ple plume imagery overlaid on satellite visible imagery shown in Fig. 1. The same facility  
124 was observed by both AVIRIS-NG and GML on different dates. In (a), two possible gas  
125 concentration peaks are not quite distinguishable, whereas in (b), multiple GML plumes are  
126 visible. GML pins mark localization of point sources with a precision of 2 m, which roughly  
127 corresponds to the size of typical production equipment. Asynchronous detections at these  
128 locations must be localized to within 2 m to count toward the same emission source. For  
129 CM, by contrast, all emitters within 150 m are aggregated to the same source. This tends  
130 to increase source-by-source emission rates because multiple emitters are summed to obtain  
131 the reported source rate. For comparison on an equal basis with CM, GML detections can  
132 also be aggregated to 150 m diameter groups. Cases where spatial aggregation is performed

133 are labeled in the analysis. Further details of GML spatial aggregation are given in Sect. S1.  
134 Further parameters, including data selection, measurement time frame, survey area, and  
135 scan repetitions were considered in compiling the data sets. Details of the data compilation  
136 are given in Sect. S2. Statistical tests are run as a check on the assumption that GML and  
137 CM data sets sample the same distribution (Sect. S3).

## 138 **Results**

139 After alignment, we combine the CM and GML data sets to obtain a joint model of the emis-  
140 sion rate distribution. We describe results in terms of the detection density and cumulative  
141 emission rate distribution. The detection sensitivity of the CM campaign is quantified by  
142 comparing the CM detection density to the joint model function, and the share of the cumu-  
143 lative emission rate measured by each campaign (scaled by sample size) is also inferred by  
144 comparing to the model. We first run the analysis on facility-sized sources (150 m diameter)  
145 and then repeat the process on single-emission sources. This highlights differences between  
146 the distributions due to spatial aggregation. Results from the CM 2020-21 campaigns are  
147 also shown.

### 148 **Facility-sized aggregated (150 m) emission sources**

149 As a first step to joint analysis, we establish a comparison domain supported by both the  
150 GML and CM samples. Sensitivity limits associated with each sample determine that emis-  
151 sion sources below the full detection limit (FDL) will be detected with diminishing probability  
152 as the emission rate decreases. The probability of detection (POD) for a given source can be  
153 characterized in detail as a function of emission rate, wind speed, and flight altitude using  
154 controlled release data in a robust Bayesian formalism.<sup>28</sup> In this work we take a simple ap-  
155 proach to restrict the emission rate domain to rates above the greater FDL of both samples.  
156 For the GML and CM samples, the limiting FDL is set by CM. We choose  $x_L = 600$  kg/h



157 as the effective FDL of the CM measurements. Accuracy of the declared FDL is not critical  
 158 as long as it is large enough to avoid introducing observations at significantly reduced POD.  
 159 All distributions are presented in the single-scan equivalent form described in Sect. S2.4.1,  
 160 which can be understood as a distribution on a characteristic emission rate from a single  
 161 observation of a given source, subject to detection sensitivity limits of the measurement cam-  
 162 paign. The characteristic emission rate approximates an instantaneous source emission rate  
 163 that would be observed in a single overflight; spatial aggregation and multiple overflights  
 164 effectively sum and average the rate across observations of the source.

165 Before fitting the data to obtain a joint distribution, we run a preliminary check on  
 166 the sample distributions using a hypothesis test based on the Kolmogorov-Smirnov (K-S)  
 167 statistic. The test is meant to show whether the GML and CM samples differ significantly  
 168 above the CM FDL, that is, in the heavy tail portion of the distribution. The outcome of the  
 169 test does not oppose the assumption that GML and CM samples follow the same distribution  
 170 (Sect. S3).

171 We next create a model of the distribution that represents both samples. The model  
 172 density function is taken to follow a generalized lognormal distribution,

$$p(x) \propto \exp\left(-\left|\frac{x - x_0}{b}\right|^m\right), \quad (1)$$

173 where  $x$  is the base-10 logarithm of the emission rate and  $x_0$ ,  $b$ , and  $m$  are fit parameters  
 174 where  $b > 0$  and  $m > 0$ . Integration over the range  $x_L \leq x < \infty$  yields the survival function

$$S(x) = \frac{1 - \operatorname{sgn}(x - x_0)\Gamma\left[\left(|x - x_0|/b\right)^m, \frac{1}{m}\right]}{1 - \operatorname{sgn}(x_L - x_0)\Gamma\left[\left(|x_L - x_0|/b\right)^m, \frac{1}{m}\right]}, \quad (2)$$

175 which has been adapted to the integration range and direction so that  $\lim_{x \rightarrow \infty} S(x) = 0$   
 176 and  $S(x_L) = 1$ . In the special case where  $m = 2$ , the generalized lognormal distribution is  
 177 simply lognormal. In either case, the fit parameters are jointly optimized using maximum  
 178 likelihood estimation (MLE). With the joint likelihood function given in Sect. S4, the samples

179 can be fit jointly below their respective FDLs. A nominal value of  $x_L = 3$  kg/h is chosen  
180 for the GML FDL for equipment-sized sources, consistent with the sensitivity of 2 kg/h  
181 (90% POD) mentioned in the Methods section. For facility-sized sources, this is increased to  
182  $x_L = 10$  kg/h to avoid underestimating the FDL, since spatial aggregation increases source  
183 emission rates. The MLE fitting process accounts for differences in sample size so the source  
184 densities are compared without requiring normalization based on survey size or number of  
185 overflights.

186 Several candidate fits are considered. The joint fit is compared to single-sample fits  
187 using lognormal and generalized lognormal forms for the density function. The purpose is to  
188 confirm that the joint fit better represents the two samples and to choose a model function  
189 that more accurately represents the two samples, particularly with respect to the “tailedness”  
190 of the distribution determined by  $m$  in Eq. 1. After obtaining fit parameters, the candidate  
191 models are assessed for relative likelihood of information loss using the Akaike information  
192 criterion (AIC).<sup>32</sup> The AIC comparison shows that the joint lognormal fit is optimal for 150 m  
193 emission sources (GML with CM 2019 or CM 2020-21), whereas a generalized lognormal  
194 model is preferred for equipment-sized emitters (GML with CM 2019;  $m = 1.619$ ). Details  
195 of the AIC analysis are given in Sect. S5. Best fit parameters for the models are shown in  
196 Table S1. Those from the optimal model provide the current best known representation of  
197 the distribution based on the GML and CM data.

198 With fit parameters obtained from the joint likelihood analysis, the resulting density  
199 function is shown in Fig. 2. Survey detections are binned by emission rate and the entire  
200 sample is scaled to a reference total of 1000 detected sources above the CM FDL. Error bars  
201 are placed at  $\pm 2p_{\text{bin}}/\sqrt{n_{\text{bin}}}$ , where  $p_{\text{bin}}$  is the density value of the bin and  $n_{\text{bin}}$  is the count  
202 of emission sources in the bin. Confidence bounds for the model fit are calculated using  
203 the likelihood ratio (LR) method at 5% rejection. The bounds consist of the most extreme  
204 value of the distribution function at every emission rate among the locus of solutions on the  
205 rejection contour. Fit agreement and scale factors are described in Sect. S6.

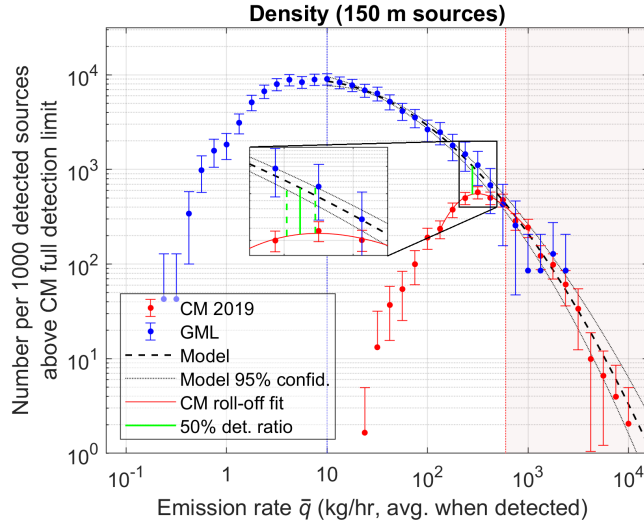


Figure 2: CM 2019 and GML emission source density as a function of emission rate, where sources have a 150 m diameter aggregation area. Zoomed in view near the sensitivity limit (inset) shows the 50% detection ratio with respect to model function and its confidence bounds.

206 Though the three traces in Fig. 2 (CM 2019, GML, and model) agree above the CM FDL,  
 207 CM detection density diminishes rapidly at emission rates below the full detection limit. By  
 208 comparing the model to the CM detection distribution around the roll-off region using an  
 209 error-weighted cubic polynomial fit of the binned data, the 50% detection ratio is placed at  
 210 280 [256, 309] kg/h, where the confidence interval (CI) is found by comparing to the 95% CI  
 211 of the model fit, neglecting error in the cubic polynomial estimating the roll-off, as shown in  
 212 the inset. This resulting sensitivity is considerably higher than the detection limit quoted by  
 213 Cusworth et al. at 10-20 kg/h but is consistent with a previous estimate of the sensitivity  
 214 in the range 100-300 kg/h.<sup>23</sup> Without compensation, reduced POD leads to a significant  
 215 underrepresentation of emission sources below the sensitivity. For example, comparing the  
 216 detection density of CM to GML binned data at 100 kg/h shows that emission sources at this  
 217 rate are in fact 14 times more common than the CM data would suggest. The CM campaign  
 218 can be expected to underestimate both the fraction of facilities with emissions and the total  
 219 emission rate for the facilities surveyed because of its sensitivity limit.

220 Controlled release measurements could confirm the sensitivity findings reported in this

221 work. Alignment on flight altitude and on-the-ground properties of the sources observed in  
222 the campaign, such as varieties of ground cover, would need to be considered. Moreover, the  
223 effects of spatial aggregation would need to be accounted for to achieve the same measure of  
224 “realized” detection sensitivity for the source definition used in the campaign.

## 225 **Equipment-sized emission sources**

226 Although the above results for 150 m sources show that emission rates less than  $\sim 300$  kg/h  
227 are underrepresented in the CM detection density, a further increase in density of lower  
228 emission rates occurs when sources are resolved to equipment size scale ( $\sim 2$  m). Facility-  
229 aggregated emission rates tend to be higher than equipment rates because co-located emitters  
230 on a site count toward the same emission source. Equipment-sized source resolution tends to  
231 be more practical for both bottom-up emissions modeling and identification for leak detection  
232 and repair.

233 To obtain the equipment-scale emission distribution, GML detections are considered in  
234 their native resolution ( $\sim 2$  m) and not aggregated to 150 m. Since CM sources are not  
235 reported at finer resolution, we instead manually filter them based on associated plume  
236 imagery<sup>31</sup> to include only sources with a single point emission (see details in Sect. S7).

237 The detection density for equipment-sized sources is shown in Fig. 3 with facility (150 m)  
238 detection density traces from Fig. 2 reproduced for comparison. At mid-range emission rates  
239 ( $\sim 3$ -300 kg/h), density is significantly higher for equipment-sized sources than for facility-  
240 sized sources. For example, comparing the two GML traces at 10 kg/h shows that equipment  
241 sources at this emission rate are observed eight times more frequently than 150 m ones.  
242 Filters applied to the CM data set do not appear to distort the distribution appreciably  
243 above the CM FDL. For other CM distributions (CM 2019 single emitters, CM 2020-21  
244 150 m sources) CM detection sensitivity is assessed in a similar manner (Sect. S8).

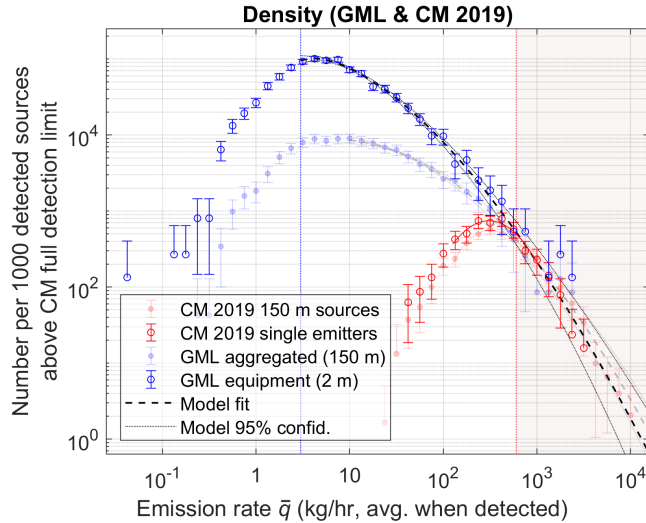


Figure 3: Density of detected emission sources with both 150 m aggregation diameter and no aggregation (single emitters), plotted together on the same axes.

## 245 Cumulative emission rate distribution

246 The density function weighted by emission rate can be integrated to yield the cumulative  
 247 emission rate distributions shown in Fig. 4. For measured samples, the cumulative sum is  
 248 given by Eq. S2 (single-scan equivalent). Results for CM 2019 (150 m sources and single  
 249 emitter sources) are shown in this section; cumulative emission rates for CM 2020-21 are  
 250 shown in Sect. S9.

251 Expected error due to sample variation is shown in the plot. Error bounds show the 2.5  
 252 and 97.5 percentiles of the sample variation for an equivalently sized data set with the same  
 253 number of detections above the corresponding FDL, assuming the best-fit model represents  
 254 the “true” distribution. They are found by running a Monte Carlo simulation of random  
 255 sets of detections drawn from the model density function (see Sect. S10). Sample error from  
 256 sources with emission rates below each FDL is neglected, as is instrument quantification  
 257 error. Sample variation in the heavy tail is responsible for much of the sample error along  
 258 the entire trace. The relatively infrequent emitters in this region have a disproportionately  
 259 large impact on cumulative emissions.

260 The fractional total emission rate measured in each survey can be found by comparing

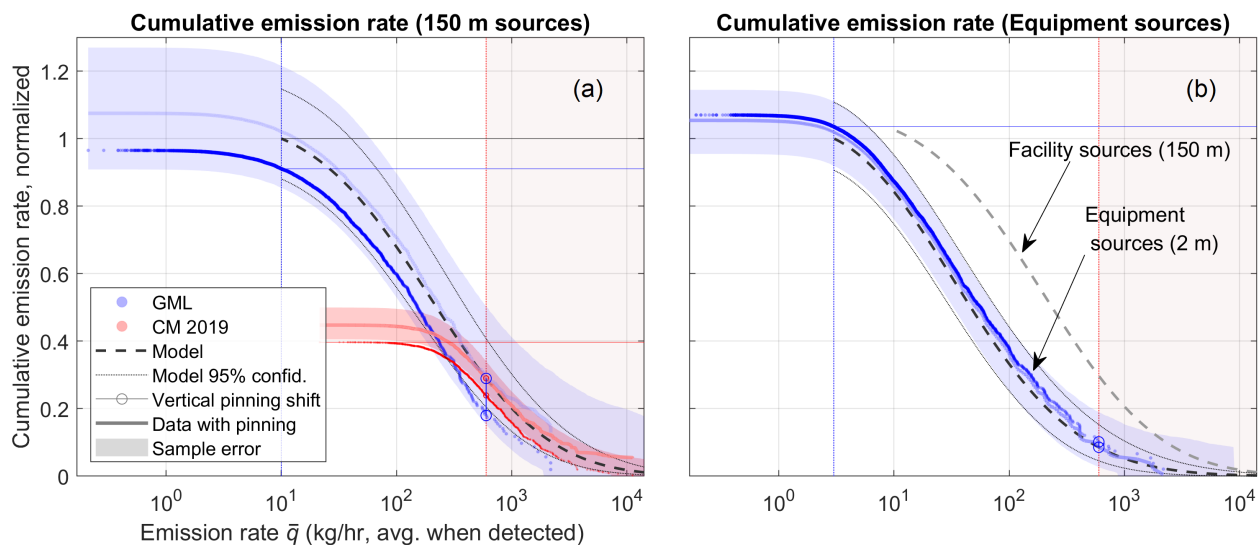


Figure 4: Cumulative emission rate distribution of (a) 150 m aggregated emission sources (GML and CM 2019) and (b) equipment sources (GML only). Error bounds (shaded regions) describe predicted sample variation. Model distribution from (a) is reproduced in (b) for comparison. All traces are normalized to equivalent campaign scale (spatial area, number of overflights). In (b), the “facility sources” model function is multiplied by the ratio of the quantity  $c(10 \text{ kg/h})/c(0)$  for each sample (see Eq. S2, single-scan equivalent) so that cumulative emissions are comparable between traces. Vertically shifted copies of survey data pinned to the value of the model distribution at the CM FDL guide the eye, suggesting the shape of the measured distribution supposing sample error above the CM FDL were suppressed.

261 the cumulative emission rate of each sample to the model function. Since the model does  
262 not extend below the GML FDL (due to the onset of sub-unity POD), we read cumulative  
263 rates at this threshold (10 kg/h for 150 m sources, 3 kg/h for equipment sources) rather  
264 than at the top of the curves. Comparing each sample to the model and its 95% CI, GML  
265 is estimated to have measured 91.1% [79.4%, 103.4%] of the total emission rate from 150 m  
266 sources above 10 kg/h and CM is estimated to have measured 39.7% [34.6%, 45.1%]. For  
267 equipment-scale sources, GML measured 103.6% [93.5%, 114.2%] of the cumulative emission  
268 rate above 3 kg/h.

269 In the case of 150 m sources, both CM 2019 and GML appear to have undermeasured  
270 the heavy tail compared to the model distribution. This can be seen from the cumulative  
271 emission rates falling below the model in Fig. 4a. In fact, the measured distribution lies  
272 outside the estimated sample error, which could be explained by a departure from lognormal  
273 behavior above source emission rates of  $10^{3.4}$  kg/h (see Sect. S6). The lower than expected  
274 cumulative emissions is consistent with a sharp drop in the measured CM 2019 survival  
275 function at  $10^{3.5}$  kg/h as shown in the inset of Fig. S8. By comparing the CM measured  
276 distribution to the model function in Fig. 4a, it can be seen that most of the CM-model error  
277 is indeed inherited from emission sources above  $10^{3.5}$  kg/h. This suggests that either the  
278 lognormal distribution does not describe the true emission rate distribution above  $10^{3.5}$  kg/h  
279 despite working well below it, or that the anomaly in CM 2019 data at  $10^{3.5}$  kg/h might be  
280 explained by undersampling, systematic error, or failure of invariance assumptions mentioned  
281 in Sect. S2. In any case, further measurements of the distribution would more clearly resolve  
282 this part of the heavy tail and explain the discrepancy.

283 Without POD compensation, missed emissions below the detection sensitivity of a given  
284 campaign raise the apparent threshold responsible for a given share of the total emission rate.  
285 For example, according to CM 2019 data alone, 90% of the total emission rate is contributed  
286 by facilities with rates above 249 kg/h, whereas in the GML distribution the 90% facility  
287 rate is 16.9 kg/h. In fact, the true 90% threshold will be even lower because emission sources

288 below GML detection sensitivity are underrepresented in the GML data set.

289 In addition, spatial aggregation of emission sources shifts (and reshapes) the entire curve  
290 to larger emission rates. Comparing the model curves in Fig. 4b shows that the 150 m source  
291 curve is shifted to the right of the equipment-level source curve by roughly a factor of 3-5  
292 over most of the domain. The 90% threshold for the total detected emission rate shifts from  
293 16.9 kg/h to 6.0 kg/h on the GML data traces. The shift toward smaller emission rates  
294 can be significant, meaning that measured distributions and sensitivity thresholds should be  
295 interpreted at the specified spatial aggregation level, and not directly compared if aggregation  
296 is different.

297 Comparing the CM and GML distributions shows that the total methane emission rate  
298 from O&G production infrastructure in the survey region is significantly greater than pre-  
299 viously reported, with GML measuring 2.3 times that measured in the CM 2019 campaigns  
300 (and also 2.3 times that in the CM 2020-21 campaigns; see Sect. S9). If observation of emis-  
301 sions is viewed as an ergodic process, then the cumulative emission rate distributions shown  
302 in Figs. 4 and S11 may be seen as representative of total average emission rate for production  
303 infrastructure in the survey region. In this case, proportions of the total emission rate from  
304 the plots can be compared to measurements of regional methane flux. Based on top-down  
305 inversion from satellite measurements of regional methane flux, Cusworth et al. estimated  
306 that sources measured in the CM 2019 survey represent 59% (CM2020-21: 49%, where frac-  
307 tions for each of the three campaigns are weighted by survey area) of the total methane  
308 emission rate in the survey region.<sup>22</sup> This estimate is somewhat higher than the proportion  
309 of cumulative emission rate measured by CM 2019 compared to GML ( $1/2.3 = 43\%$ ). If  
310 emission sources below the GML FDL were represented at their true density rather than  
311 detection density, this proportion would further decrease.



## 312 **Conclusion**

313 In summary, GML detection data extends the measured emission rate distribution for Per-  
314 mian Basin O&G production infrastructure beyond CM sensitivity limits by roughly two  
315 orders of magnitude. In joint analysis, intensive sampling of the heavy tail by CM is comple-  
316 mented by GML’s higher detection sensitivity. In the region surveyed, facility-sized emission  
317 sources with rates below the CM detection sensitivity (280 kg/h at 50% POD) contribute  
318 67% of the total emission rate from sources with rates above 10 kg/h. The density of  
319 these sources, and their constituent equipment-size emission sources (at rates above 3 kg/h),  
320 was measured without POD degradation by GML. According to the GML sample with-  
321 out POD correction, 90% of the total cumulative emission rate measured originates from  
322 equipment-sized sources with rates larger than 6.0 kg/h. This threshold rate would become  
323 even smaller if sources below 3 kg/h were measured at their true density rather than at POD  
324  $< 1$ . Emissions monitoring campaigns require both high sensitivity and intensive sampling  
325 to accurately capture the emissions distribution.

## 326 **Acknowledgement**

327 Bridger Photonics thanks the Advanced Research Program Agency – Energy (ARPA-E)  
328 MONITOR program and the Montana Board of Research and Commercialization Technology  
329 (MBRCT) for supporting the original development of GML hardware and analytics.

## 330 **Supporting Information Available**

331 The following data files are provided with this manuscript:

- 332 • GML methane emission source detection data at 150 m spatial aggregation (\*.csv).
- 333 • GML methane emission source detection data at 2 m spatial aggregation (\*.csv).

- 334 • Single-emitter classification of CM 2019 plume images (\*.csv).
- 335 • Geographic polygons bounding GML data set (\*.kml).

## 336 References

- 337 (1) Forster, P.; Storelvmo, T.; Armour, K.; Collins, W.; Dufresne, J.-L.; Frame, D.;  
338 Lunt, D. J.; Mauritsen, T.; Palmer, M. D.; Watanabe, M.; Wild, M.; Zhang, H. In *Cli-*  
339 *mate Change 2021: The Physical Science Basis. Contribution of Working Group I to the*  
340 *Sixth Assessment Report of the Intergovernmental Panel on Climate Change*; Masson-  
341 Delmotte, V., Zhai, P., Pirani, A., Connors, S. L., Pean, C., Berger, S., Caud, N.,  
342 Chen, Y., Goldfarb, L., Gomis, M. I., Huang, M., Leitzell, K., Lonnoy, E., Matthews, J.  
343 B. R., Maycock, T. K., Waterfield, T., Yelekci, O., Yu, R., Zhao, B., Eds.; Cambridge  
344 University Press, 2021; Chapter The Earth's Energy Budget, Climate Feedbacks and  
345 Climate Sensitivity, pp 923–1054, see Table 7.15.
- 346 (2) Szopa, S.; Naik, V.; Adhikary, P.; Berntsen, T.; Collins, W. D.; Fuzzi, S.; Gallardo, A.;  
347 Kiendler-Scharr, Z.; Klimont, H.; Liao, N.; Under, N.; Zanis, P. In *Climate Change*  
348 *2021: The Physical Science Basis. Contribution of Working Group I to the Sixth Assess-*  
349 *ment Report of the Intergovernmental Panel on Climate Change*; Masson-Delmotte, V.,  
350 Zhai, P., Pirani, A., Connors, S. L., Pean, C., Berger, S., Caud, N., Chen, Y., Gold-  
351 farb, L., Gomis, M. I., Huang, M., Leitzell, K., Lonnoy, E., Matthews, J. B. R., May-  
352 cock, T. K., Waterfield, T., Yelekci, O., Yu, R., Zhao, B., Eds.; Cambridge University  
353 Press, 2021; Chapter Short-lived Climate Forcers, pp 817–922, see Fig. 6.16.
- 354 (3) Brandt, A. R.; Heath, G. A.; Kort, E. A.; O'Sullivan, F.; Pétron, G.; Jordaan, S. M.;  
355 Tans, P.; Wilcox, J.; Gopstein, A. M.; Arent, D.; Wofsy, S.; Brown, N. J.; Bradley, R.;  
356 Stucky, G. D.; Eardley, D.; Harriss, R. Methane leaks from North American natural  
357 gas systems. *Science* **2014**, *343*, 733–735.

- 358 (4) Allen, D. T. Methane emissions from natural gas production and use: Reconciling  
359 bottom-up and top-down measurements. *Current Opinion in Chemical Engineering*  
360 **2014**, *5*, 78–83.
- 361 (5) Zimmerle, D. J.; Williams, L. L.; Vaughn, T. L.; Quinn, C.; Subramanian, R.; Dug-  
362 gan, G. P.; Willson, B.; Opsomer, J. D.; Marchese, A. J.; Martinez, D. M.; Robin-  
363 son, A. L. Methane Emissions from the Natural Gas Transmission and Storage System  
364 in the United States. *Environmental Science and Technology* **2015**, *49*, 9374–9383.
- 365 (6) Marchese, A. J.; Vaughn, T. L.; Zimmerle, D. J.; Martinez, D. M.; Williams, L. L.;  
366 Robinson, A. L.; Mitchell, A. L.; Subramanian, R.; Tkacik, D. S.; Roscioli, J. R.;  
367 Herndon, S. C. Methane Emissions from United States Natural Gas Gathering and  
368 Processing. *Environmental Science and Technology* **2015**, *49*, 10718–10727.
- 369 (7) Alvarez, R. A.; Zavala-Araiza, D.; Lyon, D. R.; Allen, D. T.; Barkley, Z. R.;  
370 Brandt, A. R.; Davis, K. J.; Herndon, S. C.; Jacob, D. J.; Karion, A.; Kort, E. A.;  
371 Lamb, B. K.; Lauvaux, T.; Maasakkers, J. D.; Marchese, A. J.; Omara, M.;  
372 Pacala, S. W.; Peischl, J.; Robinson, A. L.; Shepson, P. B.; Sweeney, C.; Townsend-  
373 Small, A.; Wofsy, S. C.; Hamburg, S. P. Assessment of methane emissions from the U.S.  
374 oil and gas supply chain. *Science* **2018**, *361*, 186–188.
- 375 (8) Omara, M.; Zimmerman, N.; Sullivan, M. R.; Li, X.; Ellis, A.; Cesa, R.; Subrama-  
376 nian, R.; Presto, A. A.; Robinson, A. L. Methane Emissions from Natural Gas Produc-  
377 tion Sites in the United States: Data Synthesis and National Estimate. *Environmental*  
378 *Science and Technology* **2018**, *52*, 12915–12925.
- 379 (9) Rutherford, J. S.; Sherwin, E. D.; Ravikumar, A. P.; Heath, G. A.; Englander, J.;  
380 Cooley, D.; Lyon, D.; Omara, M.; Langfitt, Q.; Brandt, A. R. Closing the methane gap  
381 in US oil and natural gas production emissions inventories. *Nature Communications*  
382 **2021**, *12*, 4715.

- 383 (10) Duren, R.; Thorpe, A.; McCubbin, I. *The California Methane Survey*; 2020; California  
384 Energy Commission. Publication Number: CEC-500-2020-047.
- 385 (11) Harriss, R.; Alvarez, R. A.; Lyon, D.; Zavala-Araiza, D.; Nelson, D.; Hamburg, S. P.  
386 Using Multi-Scale Measurements to Improve Methane Emission Estimates from Oil  
387 and Gas Operations in the Barnett Shale Region, Texas. *Environmental Science and*  
388 *Technology* **2015**, *49*, 7524–7526.
- 389 (12) Vaughn, T. L.; Bell, C. S.; Pickering, C. K.; Schwietzke, S.; Heath, G. A.; Pétron, G.;  
390 Zimmerle, D. J.; Schnell, R. C.; Nummedal, D. Temporal variability largely explains  
391 top-down/bottom-up difference in methane emission estimates from a natural gas pro-  
392 duction region. *Proceedings of the National Academy of Sciences of the United States*  
393 *of America* **2018**, *115*, 11712–11717.
- 394 (13) Johnson, M.; Tyner, D.; McCole, E.; Conrad, B.; Milani, Z.; Seymour, S.; Roth, C.;  
395 Burt, D.; Festa-Bianchet, S.; Mohammadikharkeshi, M.; Kirby, F.; Szekeres, A. Ap-  
396 plication of Airborne LiDAR Measurements to Create Measurement-Based Methane  
397 Inventories in the Canadian Upstream Oil & Gas Sector. American Geophysical Union  
398 Fall Meeting 2021. 2021; pp GC24D–03.
- 399 (14) Peischl, J.; Eilerman, S. J.; Neuman, J. A.; Aikin, K. C.; de Gouw, J.; Gilman, J. B.;  
400 Herndon, S. C.; Nadkarni, R.; Trainer, M.; Warneke, C.; Ryerson, T. B. Quantifying  
401 Methane and Ethane Emissions to the Atmosphere From Central and Western U.S. Oil  
402 and Natural Gas Production Regions. *Journal of Geophysical Research: Atmospheres*  
403 **2018**, *123*, 7725–7740.
- 404 (15) Robertson, A. M.; Edie, R.; Field, R. A.; Lyon, D.; McVay, R.; Omara, M.; Zavala-  
405 Araiza, D.; Murphy, S. M. New Mexico Permian basin measured well pad methane  
406 emissions are a factor of 5-9 times higher than U.S. EPA estimates. *Environmental*  
407 *Science and Technology* **2020**, *54*, 13926–13934.

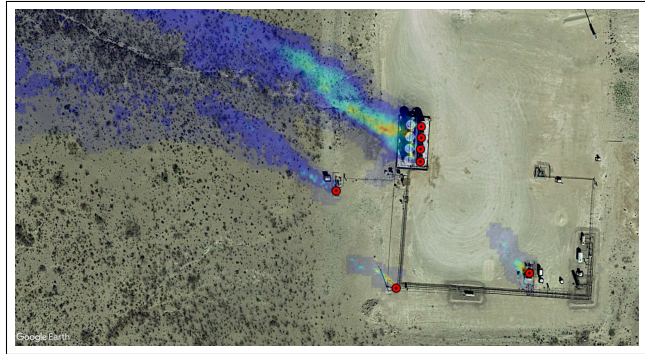
- 408 (16) Popova, O.; Long, G. *Advances in technology led to record new well productiv-*  
409 *ity in the Permian Basin in 2021*; 2022; U.S. Energy Information Administration,  
410 <https://www.eia.gov/todayinenergy/detail.php?id=54079>.
- 411 (17) Schneising, O.; Buchwitz, M.; Reuter, M.; Vanselow, S.; Bovensmann, H.; Burrows, J. P.  
412 Remote sensing of methane leakage from natural gas and petroleum systems revisited.  
413 *Atmospheric Chemistry and Physics* **2020**, *20*, 9169–9182.
- 414 (18) Zhang, Y.; Gautam, R.; Pandey, S.; Omara, M.; Maasakkers, J. D.; Sadavarte, P.;  
415 Lyon, D.; Nesser, H.; Sulprizio, M. P.; Varon, D. J.; Zhang, R.; Houweling, S.; Zavala-  
416 Araiza, D.; Alvarez, R. A.; Lorente, A.; Hamburg, S. P.; Aben, I.; Jacob, D. J. Quanti-  
417 fying methane emissions from the largest oil-producing basin in the United States from  
418 space. *Science Advances* **2020**, *6*, eaaz5120.
- 419 (19) Varon, D. J.; Jacob, D. J.; Hmiel, B.; Gautam, R.; Lyon, D. R.; Omara, M.; Sul-  
420 prizio, M.; Shen, L.; Pendergrass, D.; Nesser, H.; Qu, Z.; Barkley, Z. R.; Miles, N. L.;  
421 Richardson, S. J.; Davis, K. J.; Pandey, S.; Lu, X.; Lorente, A.; Borsdorff, T.;  
422 Maasakkers, J. D.; Aben, I. Continuous weekly monitoring of methane emissions  
423 from the Permian Basin by inversion of TROPOMI satellite observations. preprint at  
424 <https://acp.copernicus.org/preprints/acp-2022-749/>.
- 425 (20) Sherwin, E.; Rutherford, J.; Zhang, Z.; Chen, Y.; Wetherley, E.; Yakovlev, P.;  
426 Berman, E.; Jones, B.; Thorpe, A.; Ayasse, A.; Duren, R.; Brandt, A.; Cusworth, D.  
427 Quantifying oil and natural gas system emissions using one million aerial site measure-  
428 ments. preprint at <https://doi.org/10.21203/rs.3.rs-2406848/v1>.
- 429 (21) Cusworth, D. H.; Duren, R. M.; Thorpe, A. K.; Olson-Duvall, W.; Heckler, J.; Chap-  
430 man, J. W.; Eastwood, M. L.; Helmlinger, M. C.; Green, R. O.; Asner, G. P.; Den-  
431 nison, P. E.; Miller, C. E. Intermittency of Large Methane Emitters in the Permian  
432 Basin. *Environmental Science and Technology Letters* **2021**, *8*, 567–573.

- 433 (22) Cusworth, D. H.; Thorpe, A. K.; Ayasse, A. K.; Stepp, D.; Heckler, J.; Asner, G. P.;  
434 Miller, C. E.; Yadav, V.; Chapman, J. W.; Eastwood, M. L.; Green, R. O.; Hmiel, B.;  
435 Lyon, D. R.; Duren, R. M. Strong methane point sources contribute a disproportionate  
436 fraction of total emissions across multiple basins in the United States. *Proceedings of*  
437 *the National Academy of Sciences* **2022**, *119*, e2202338119.
- 438 (23) Chen, Y.; Sherwin, E. D.; Berman, E. S. F.; Jones, B. B.; Gordon, M. P.; Wether-  
439 ley, E. B.; Kort, E. A.; Brandt, A. R. Quantifying regional methane emissions in the  
440 New Mexico Permian Basin with a comprehensive aerial survey. *Environmental Science*  
441 *and Technology* **2022**, *56*, 4317–23.
- 442 (24) Johnson, M. R.; Tyner, D. R.; Szekeres, A. J. Blinded evaluation of airborne methane  
443 source detection using Bridger Photonics LiDAR. *Remote Sensing of Environment*  
444 **2021**, *259*, 112418.
- 445 (25) Bell, C.; Rutherford, J.; Brandt, A.; Sherwin, E.; Vaughn, T.; Zimmerle, D. Single-blind  
446 determination of methane detection limits and quantification accuracy using aircraft-  
447 based LiDAR. *Elementa: Science of the Anthropocene* **2022**, *10*, 00080.
- 448 (26) National Weather Service, Midland Texas Monthly Wind Averages. [Data set].  
449 [https://www.weather.gov/maf/cli\\_maf\\_winds](https://www.weather.gov/maf/cli_maf_winds) (Retrieved 2022-Dec-12).
- 450 (27) Thorpe, A.; Frankenberg, C.; Aubrey, A.; Roberts, D.; Nottrott, A.; Rahn, T.;  
451 Sauer, J.; Dubey, M.; Costigan, K.; Arata, C.; Steffke, A.; Hills, S.; Haselwimmer, C.;  
452 Charlesworth, D.; Funk, C.; Green, R.; Lundeen, S.; Boardman, J.; Eastwood, M.;  
453 Sarture, C.; Nolte, S.; Mccubbin, I.; Thompson, D.; McFadden, J. Mapping methane  
454 concentrations from a controlled release experiment using the next generation airborne  
455 visible/infrared imaging spectrometer (AVIRIS-NG). *Remote Sensing of Environment*  
456 **2016**, *179*, 104–115.
- 457 (28) Conrad, B. M.; Tyner, D. R.; Johnson, M. R. Robust probabilities of detection and

- 458 quantification uncertainty for aerial methane detection: Examples for three airborne  
459 technologies. *Remote Sensing of Environment* **2023**, *288*, 113499.
- 460 (29) Duren, R. M.; Thorpe, A. K.; Foster, K. T.; Rafiq, T.; Hopkins, F. M.; Yadav, V.;  
461 Bue, B. D.; Thompson, D. R.; Conley, S.; Colombi, N. K.; Frankenberg, C.; McCub-  
462 bin, I. B.; Eastwood, M. L.; Falk, M.; Herner, J. D.; Croes, B. E.; Green, R. O.;  
463 Miller, C. E. California’s methane super-emitters. *Nature* **2019**, *575*, 180–184.
- 464 (30) Thorpe, A. K.; O’Handley, C.; Emmitt, G. D.; DeCola, P. L.; Hopkins, F. M.; Yadav, V.;  
465 Guha, A.; Newman, S.; Herner, J. D.; Falk, M.; Duren, R. M. Improved methane  
466 emission estimates using AVIRIS-NG and an Airborne Doppler Wind Lidar. *Remote*  
467 *Sensing of Environment* **2021**, *266*, 112681.
- 468 (31) Cusworth, D. Methane plumes for NASA/JPL/UArizona/ASU Sep-Nov 2019 Permian  
469 campaign. 2021; [Data set]. Zenodo. <https://doi.org/10.5281/zenodo.5610307>.
- 470 (32) Akaike, H. In *Selected Papers of Hirotugu Akaike*; Parzen, E., Tanabe, K., Kitagawa, G.,  
471 Eds.; Springer New York: New York, NY, 1998; pp 199–213.

472 TOC Graphic

473





# Supporting Information

## Extension of Methane Emission Rate Distribution for Permian Basin Oil and Gas Production Infrastructure by Aerial LiDAR

1 William M. Kunkel,\* Asa E. Carre-Burritt, Grant S. Aivazian, Nicholas C. Snow,  
Jacob T. Harris, Tagert S. Mueller, Peter A. Roos, and Michael J. Thorpe\*

*Bridger Photonics, Inc., 2310 University Way Bldg 4-4, Bozeman, MT 59715, USA*

E-mail: William.Kunkel@bridgerphotonics.com; Mike.Thorpe@bridgerphotonics.com

## 2 Contents

3	<b>Section S1: Spatial aggregation to 150 m sources</b>	<b>S2</b>
4	<b>Section S2: Data preparation and alignment</b>	<b>S3</b>
5	S2.1: Sample composition and emitter types included . . . . .	S4
6	S2.2: Spatial overlap of CM and GML samples . . . . .	S5
7	S2.3: Temporal overlap of CM and GML samples . . . . .	S6
8	S2.4: Scan repetitions . . . . .	S6
9	<b>Section S3: Kolmogorov-Smirnov test</b>	<b>S10</b>
10	<b>Section S4: Likelihood function</b>	<b>S13</b>
11	<b>Section S5: Akaike information criterion (AIC) analysis</b>	<b>S13</b>
12	<b>Section S6: Model fit and scaling</b>	<b>S14</b>

13	<b>Section S7: Equipment-scale emission source filtering</b>	<b>S18</b>
14	<b>Section S8: Density plots (CM 2019 single emitters, CM 2020-21)</b>	<b>S18</b>
15	<b>Section S9: Cumulative emission rate distribution (CM 2020-21)</b>	<b>S19</b>
16	<b>Section S10: Monte Carlo estimation of sample error</b>	<b>S21</b>
17	<b>Section S11: Exclusion of pipelines from CM data set</b>	<b>S21</b>
18	<b>References</b>	<b>S24</b>

## 19 **S1. Spatial aggregation to 150 m sources**

20 Spatial analysis of GML data is performed by first assigning an emission origin point, or  
21 “location,” to each detected plume. Detections observed at different times are associated  
22 with the same location if they are co-located within 2 m. Emission locations were spatially  
23 aggregated to 150 m sources by a clustering algorithm that iterates through a list of GML  
24 locations to build a temporary table of locations within 150 m to all other locations in the  
25 current cluster. After all unclustered locations in the list have been compared (sequentially,  
26 in fixed arbitrary order) to the temporary cluster, those in the temporary cluster are removed  
27 from the waiting list. New clusters are formed in this way until no locations remain in the  
28 waiting list.

29 GML detections can also be aggregated to “facilities” described by polygons enclosing site  
30 assets. Facility polygons represent the boundaries around actual groups of surface infras-  
31 tructure and are usually defined by the facility pad footprint. Polygons can be provided by  
32 operators based on site data or generated from aerial photography, in which case the polygon  
33 is drawn either manually or by an artificial intelligence model. A mix of AI-generated and  
34 manual polygons was used in the data set in this work. A polygon is defined for every facility  
35 on a GML flight path regardless of whether an emission is actually detected.

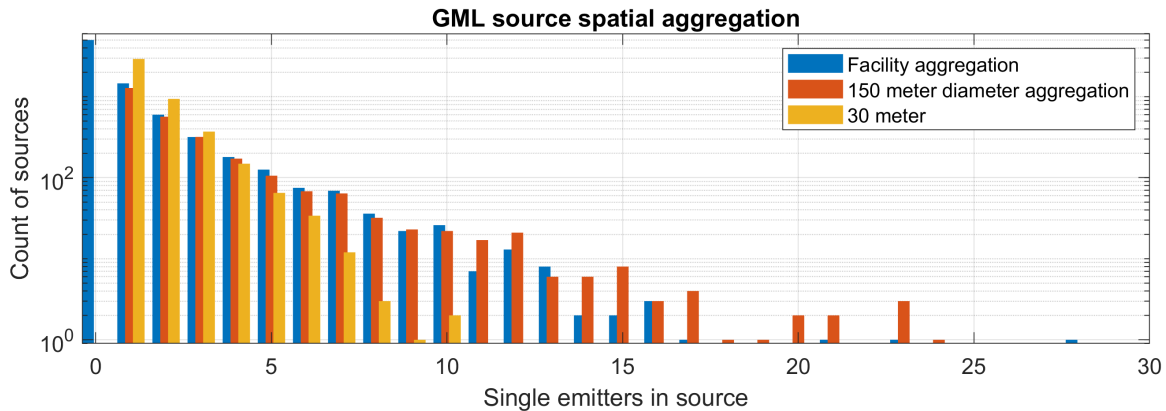


Figure S1: Histogram counting spatially aggregated sources by number of emitters in aggregation area.

36 Comparing the number of GML locations in each facility to the number per 150 m di-  
 37 ameter source shows a near correspondence between the two aggregation styles (Fig. S1),  
 38 supporting the use of 150 m aggregation to represent facility-sized sources. A smaller aggrega-  
 39 tion area (30 meters) displays a steeper roll-off in number of detection locations per source.  
 40 For GML, the proportion of facilities with at least one detection was found to be 38.3% (or  
 41 32.9% when considering only first overflights in the 15-minute scan window described in  
 42 Sect. S2.4.2), much higher than the reported 1.48% rate<sup>1</sup> of well sites in the CM 2019 cam-  
 43 paign. This difference may be explained by differences in detection sensitivity described in  
 44 the analysis.

## 45 S2. Data preparation and alignment

46 Before jointly analyzing emission detection data from diverse sources, several aspects of data  
 47 collection and data set composition must be considered. In this section we aim to address  
 48 some important aspects of data alignment, specifically (1) compilation of GML survey data  
 49 and types of emitters included, (2) spatial overlap of CM and GML surveys, (3) temporal  
 50 overlap of CM and GML surveys, and (4) influence of scan repetitions on reported emission  
 51 rates. In preparation for this work, efforts were made to directly align the data sets as  
 52 much as possible. Where data sets do not align, limited assumptions of spatial or temporal

53 invariance are needed to complete the analysis. We aim to point out where these occur in  
54 the details of the data curation process below.

## 55 **S2.1 Sample composition and emitter types included**

56 The GML sample is compiled from sets of anonymized survey data collected under contracts  
57 for client O&G operators (individuals and associations). Survey sets for compilation were  
58 chosen for geographical and temporal overlap with CM data without considering analysis  
59 results. Whereas CM campaigns blanketed entire geographic areas, GML surveys were tar-  
60 geted to client facilities. Clients were given advance notice of when scans would occur (typ.  
61 accuracy  $\pm 2$ -3 days). The sample is comprised of scans of sites belonging to 28 operators.

62 Sites included in the GML sample were in the O&G production sector and do not include  
63 midstream/distribution infrastructure. Types of infrastructure included in the GML sample  
64 consist of wells, separators, tanks, compressors, flares, vapor recovery units, generators, and  
65 facility piping. In this work, CM data have been filtered to exclude detections from O&G  
66 pipelines unless otherwise marked. In the CM 2019 data set,<sup>2</sup> measurements with all *source*  
67 *type* tags were included except for “pipeline” and “NA.” For CM 2020-21,<sup>3</sup> the accepted tags  
68 were “tank,” “well,” “compressor,” “processing,” and “refinery.” Exclusion of pipelines seems  
69 to have a negligible effect on the shape of the CM distribution, as shown in Sect. S11.

70 False positive detections can occur in GML detection data, but practically only near the  
71 GML detection limit. For emission rates more than a factor of two above the GML detection  
72 limit the likelihood of false positives is vanishingly small. GML uses a physics model of  
73 the LiDAR measurement noise processes (shot noise, photodetector noise, speckle noise) to  
74 estimate the noise on each methane concentration LiDAR measurement based on received  
75 light levels. During processing of GML data the signal to noise ratio for each measurement  
76 is used in a statistical algorithm to detect regions of elevated methane concentration. The  
77 detected regions of elevated concentration are then submitted to emitter analysis, which only  
78 assigns an emitter if a hot spot in both detection confidence and concentration is detected

79 at the upwind end of the detected plume.

## 80 S2.2 Spatial overlap of CM and GML samples

81 GML and CM 2019 samples were restricted to the GAO coverage polygons in the Delaware  
82 and Midland Basins provided in Ref. 1. Geography is shown in Fig. S2. Restriction to the  
83 GAO polygons excludes 29 out of 1756 detected facility sources in CM 2019. GML detection  
84 locations occupy a subregion of both GAO polygons. We assume that the complementary  
85 area in the GAO polygon does not significantly affect the emission rate distribution.

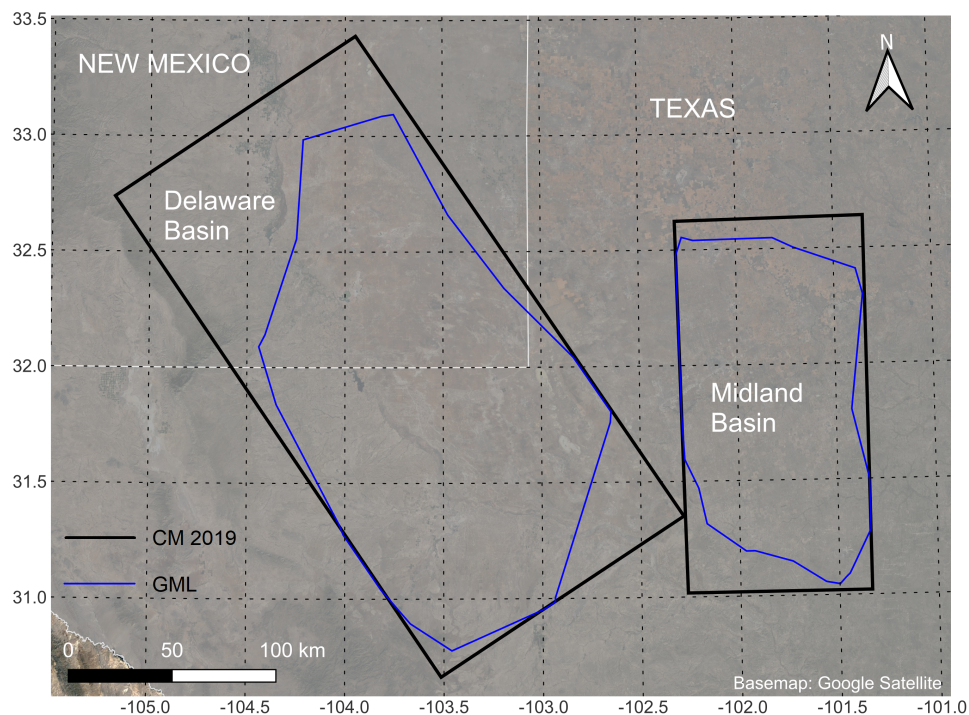


Figure S2: Geographical location of detected emissions included in the GML and CM 2019 samples. GML polygons are randomly buffered so the vertices do not correspond to detection locations.

86 Though the CM 2020-21 coverage areas<sup>4</sup> intersect the 2019 GAO polygons, they do not  
87 cover the entire area of the 2019 polygons and contain additional area outside the 2019  
88 polygons. We do not explicitly align GML and CM 2020-21 survey areas in this work, but  
89 rather assume that the emission rate distribution is roughly spatially invariant among these  
90 areas. We use the same GML data set for joint analysis with CM 2019 and CM 2020-21.

91 We apply no geographic filters to CM 2020-21, other than to select the campaigns that took  
92 place in the Permian Basin (*source ID* markers “F,” “E,” and “J” in the published data set<sup>3</sup>).

### 93 S2.3 Temporal overlap of CM and GML samples

94 A timeline of plume detections in the GML and CM measurement campaigns is shown in  
95 Fig. S3. GML scans were performed between Jan 2020 and Feb 2022, whereas the CM  
96 campaigns took place in Sept-Nov 2019 (CM 2019) and Jul 2020-Nov 2021 (CM 2020-21).  
97 Analysis in the Results section assumes stationarity in the shape of the emission rate distri-  
98 bution with time (i.e. does not change with choice of time origin). However, stationarity of  
99 the scale of the distribution is not required. The joint analysis computes separate likelihoods  
100 for each data set and scales the density and cumulative emissions traces to the total density  
101 above the CM full detection limit.

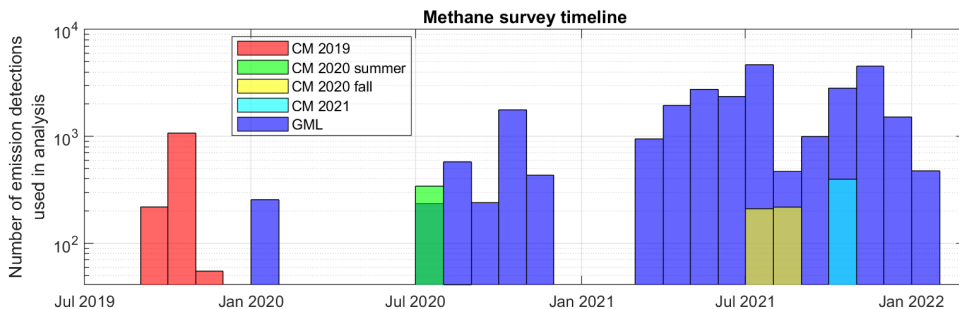


Figure S3: Plume detection counts versus time for CM and GML measurement campaigns.

### 102 S2.4 Scan repetitions

103 CM and GML campaigns were conducted with different approaches to scan repetitions.  
104 Number of scans per emission source is shown in Fig. S4. Fewer scans were performed per  
105 150 m source with GML (median: 2 scans) in comparison to CM (2019 median: 6 scans,  
106 2020-21: 4 scans). In CM campaigns, repeated scans over a given source were performed  
107 independently of previous results. No minimum number of scans was used to filter the data  
108 sets for this work. In GML surveys, repeated scans were performed only on locations where

109 an emission was detected in the first scan. This means that emissions measured by GML  
 110 were effectively found in just one scan, and repeat measurements were not independent.  
 111 Most emission sources in the CM campaign had multiple opportunities to be detected, so a  
 112 greater fraction will have been detected. To address these issues, we describe two solutions  
 113 below: how to express the distributions in a form that enables direct comparison, and how  
 114 to handle GML observations.

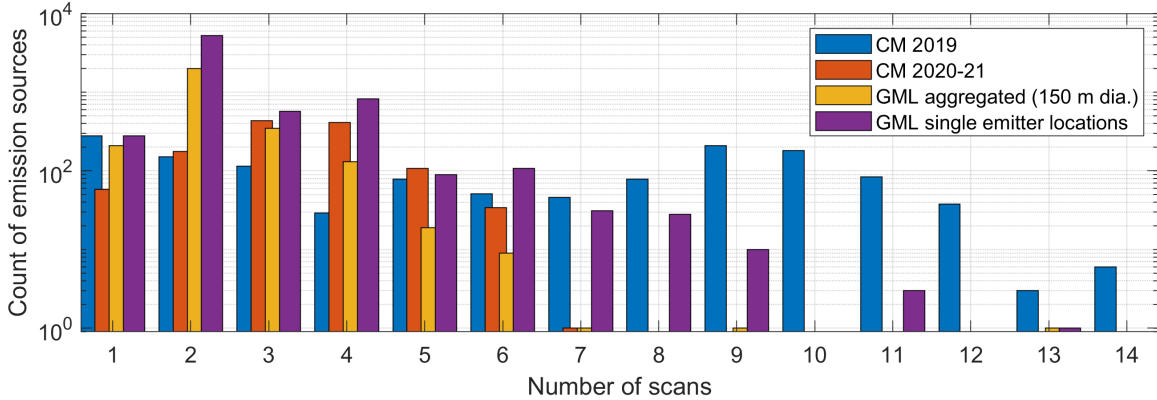


Figure S4: Histogram counting emission sources by number of scan repetitions.

### 115 S2.4.1 Transformation to single-scan equivalent

116 GML and CM distributions are expressed in a “single-scan equivalent” form for alignment.  
 117 We adopt the notation and terminology of Cusworth et al.<sup>1</sup> for the persistence-adjusted  
 118 emission rate  $q = f\bar{q}$ , where  $f$  is the observed persistence  $f = M/N$ , with  $M$  as the number  
 119 of non-zero unique detections and  $N$  as the number of scans, and  $\bar{q}$  is the mean of all non-zero  
 120 measured emission rates

$$\bar{q} = \frac{1}{M} \sum_{i=1}^M q_i, \quad (\text{S1})$$

121 where  $q_i$  is a non-zero unique emission rate measurement. For a given source emitting  
 122 intermittently at a single rate,  $\bar{q}$  should be consistent across number of measurement scans,  
 123 which aids in comparing measurements with different numbers of scans.

124 To plot emission density and cumulative emission rate on a  $\bar{q}$  axis requires further adjust-  
 125 ment using the persistence. Consider a point on the detection density function, or rather,

126 a single point in a discrete series representing detection frequency, as shown in Fig. S5a.  
 127 The persistence adjusted detection frequency (blue), where the emission rate is  $q$ , is acces-  
 128 sible only from a repetitive sample set and not from a single scan, since the persistence  $f$  is  
 129 needed to obtain  $q$ . The detection frequency can be replotted at  $\bar{q}$ , which effectively removes  
 130 the persistence from the emission rate. This results in an effectively higher emission rate  
 131 (green dashed) which overrepresents the density at this emission rate. To obtain a correctly  
 132 weighted frequency for summation, or density for integration, (red), the prevalence of the  
 133 source must be reduced by the persistence. Where the density or frequency function contains  
 134 many points, the remapping of  $q$  to  $\bar{q}$  and the persistence weighting  $f$  applies to all points  
 135 on the curve.

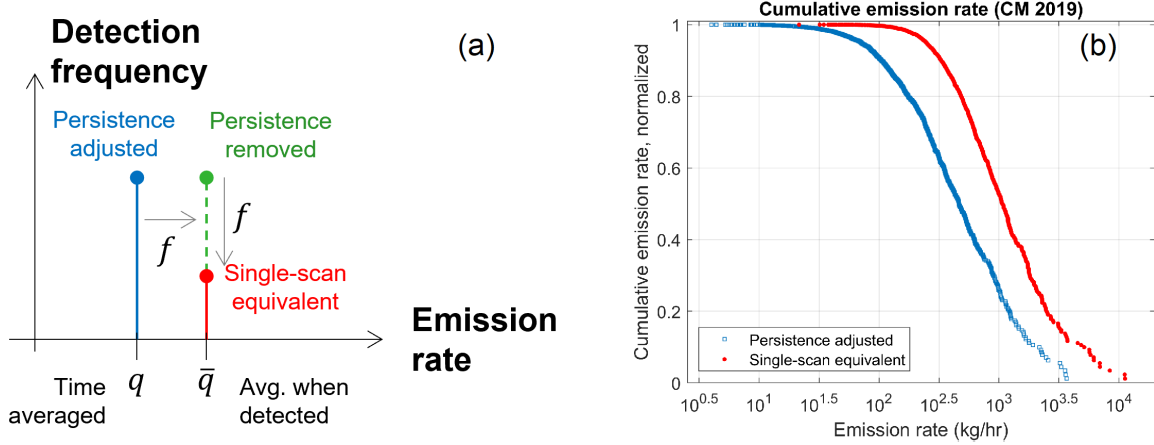


Figure S5: Transformation of emission distribution using the observed persistence  $f$ , for (a) a discrete point in a measurement series and (b) the cumulative emission rate distribution (CM 2019, 150 m sources). In both plots, emission rate on the  $x$ -axis means either  $q$  or  $\bar{q}$  as indicated.

136 Next, consider the implications for the cumulative emission rate distribution. For a finite  
 137 set of measurements, the cumulative emission rate is computed using the discrete sum

$$c(x) = \frac{1}{\sum q} \cdot \begin{cases} \sum_{q \geq x} q & \text{(persistence adjusted)} \\ \sum_{\bar{q} \geq x} f \bar{q} & \text{(single-scan equivalent)} \end{cases}, \quad (\text{S2})$$

138 where  $x$  is the emission rate. The result of Eq. S2 applied to the CM 2019 sample used



139 for analysis is shown in Fig. S5b. Different forms of the sum yield the same total emission  
 140 rate since each source contributes the same emission rate. Effectively the contributions have  
 141 been re-ordered according to the corresponding value of  $q$  or  $\bar{q}$ . As a result, the single-scan  
 142 equivalent distribution is a reshaped and horizontally shifted version of the persistence-  
 143 adjusted distribution.

144 Although this treatment conveniently transforms distributions for comparison regardless  
 145 of number of scans, the resulting distributions are not exact. Noting that the observed  
 146 persistence  $f$  is an observation of an event with probability equal to the actual source per-  
 147 sistence times the probability of detection (POD), some distortion of the distribution can be  
 148 expected where sources with  $\text{POD} < 1$  from below the FDL are shifted above it. Whereas  
 149 this affects multi-scan data sets like CM, single-scan data sets (which GML approximates)  
 150 would not be affected.

### 151 S2.4.2 GML detections

152 GML observations of a given emission source come at three different levels: overflight, loca-  
 153 tion scan, and aggregated source scan. A location scan is comprised of one or more aerial  
 154 passes (“overflights”) of an emission source seen at GML source resolution ( $\sim 2$  m). The  
 155 first measurement out of all overflights within a 15-minute time window, inclusive of mea-  
 156 surements with zero and non-zero emission rates, is selected to represent the emission rate  
 157 for the scan. Scan measurements are then converted to a persistence-adjusted rate  $q$  and  
 158 associated observed persistence  $f$  for the location. These are used to find the “average when  
 159 detected” rate  $\bar{q}$  in the same way as for the CM data, using Eq. S1.

160 For spatially aggregated sources (150 m), emission rates are found by adding the persis-  
 161 tence adjusted emission rates for each location in the source, and dividing by a composite  
 162 persistence value for the source,

$$f_{\text{agg}} = \frac{\sum_i q_{\text{loc},i} f_{\text{loc},i}}{\sum_i q_{\text{loc},i}}, \quad (\text{S3})$$

163 where  $q_{loc,i}$  is the persistence adjusted emission rate and  $f_{loc,i}$  is the observed persistence,  
 164 where both correspond to the  $i^{\text{th}}$  location in the source. In other words, the aggregated  
 165 source persistence is an average of the observed location persistence values, weighted by the  
 166 persistence-adjusted location emission rates. The average emission rate for the source, when  
 167 detected, is then calculated as  $\bar{q} = \sum_i q_{loc,i}/f_{agg}$ .

### 168 S3. Kolmogorov-Smirnov test

169 A two-sample Kolmogorov-Smirnov (K-S) test<sup>5</sup> is used to check for differences between the  
 170 GML and CW samples. This is a non-parametric test with a standard null hypothesis (no  
 171 statistically significant difference between the samples). Here the test is performed on the  
 172 survival function for a single-scan equivalent sample,

$$S(x) = \frac{\sum_{\bar{q} \geq x}^{\infty} f(\bar{q})}{\sum_{\bar{q} = x_L}^{\infty} f(\bar{q})}, \quad (\text{S4})$$

173 where  $x$  is the emission rate and  $x \geq x_L$ , with  $x_L$  as the lower bound of a range of interest,  
 174 and  $f$  is the observed persistence for a given measurement with emission rate  $\bar{q}$ . The sum is  
 175 represented as a stepwise function for the K-S test. As mentioned in the Results section, we  
 176 choose  $x_L = 600 \text{ kg h}^{-1}$  as the effective full detection limit of CM measurements.

177 The survival function of the GML and CM 2019 samples are plotted in Fig. S6. The  
 178 Kolmogorov-Smirnov (K-S) statistic shows the maximum absolute residual between the two  
 179 sample distributions. The number of measurements in the GML sample is small in this  
 180 range. In both cases the associated  $p$ -values are high and do not indicate rejection of the  
 181 null hypothesis.

182 The K-S test is also used to check the measured emission distribution for the CM 2020-21  
 183 campaigns against GML. In 2020-21, CM conducted three campaigns around the Midland  
 184 and Delaware sub-basins (2020 summer, 2021 summer, 2021 fall). Each campaign is smaller

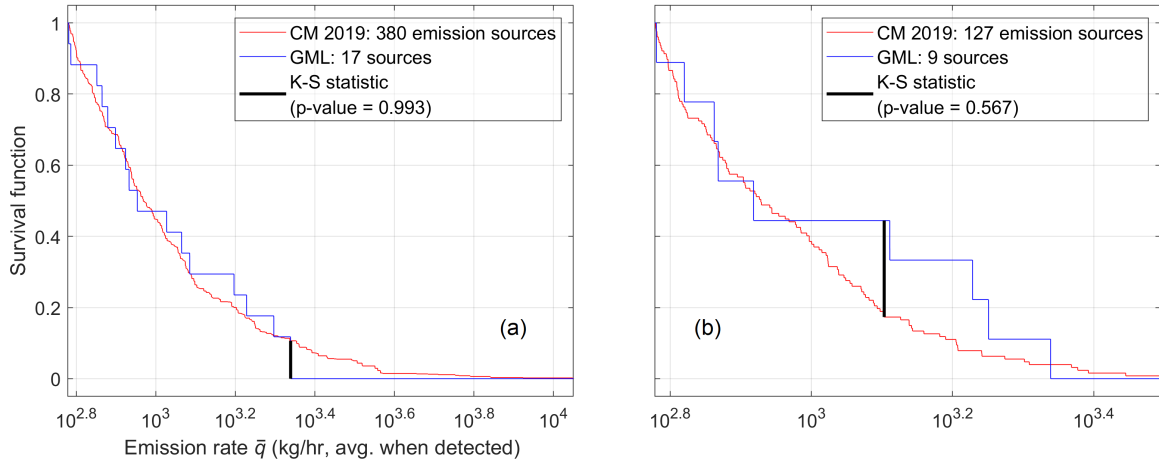


Figure S6: Survival function of single-scan equivalent CM 2019 and GML source detections above  $600 \text{ kg h}^{-1}$  where sources are defined by a (a) 150 m aggregation diameter and (b) single emitter. Kolmogorov-Smirnov (K-S) statistic and associated  $p$ -value are shown.

185 than CM 2019 in number of detections and number of overflights (see Fig. S1). Spatial  
 186 overlap among these campaigns is partial; overlap with CM 2019 is also partial.<sup>4</sup> For the  
 187 analysis in this paper, no controls for spatial overlap were used, under the assumption that  
 188 the shape of the emission distribution is spatially invariant over the CM 2019 and CM 2020-21  
 189 domains. The GML data set is unchanged whether comparing to CM 2019 or CM 2020-21.

190 Fig. S7 shows the distributions and K-S test results. For the CM 2020 campaign, a devia-  
 191 tion around  $10^{2.9} \text{ kg h}^{-1}$  is responsible for a slightly low  $p$ -value of 0.166. When grouped with  
 192 the other campaign data, however, the CM 2020 deviation no longer causes the maximum  
 193 difference in sample distributions (comparing Fig. S7a and Fig. S7d). For analysis in the  
 194 rest of this paper, all three CM 2020-21 campaigns were merged into one data set as shown  
 195 in Fig. S7d.

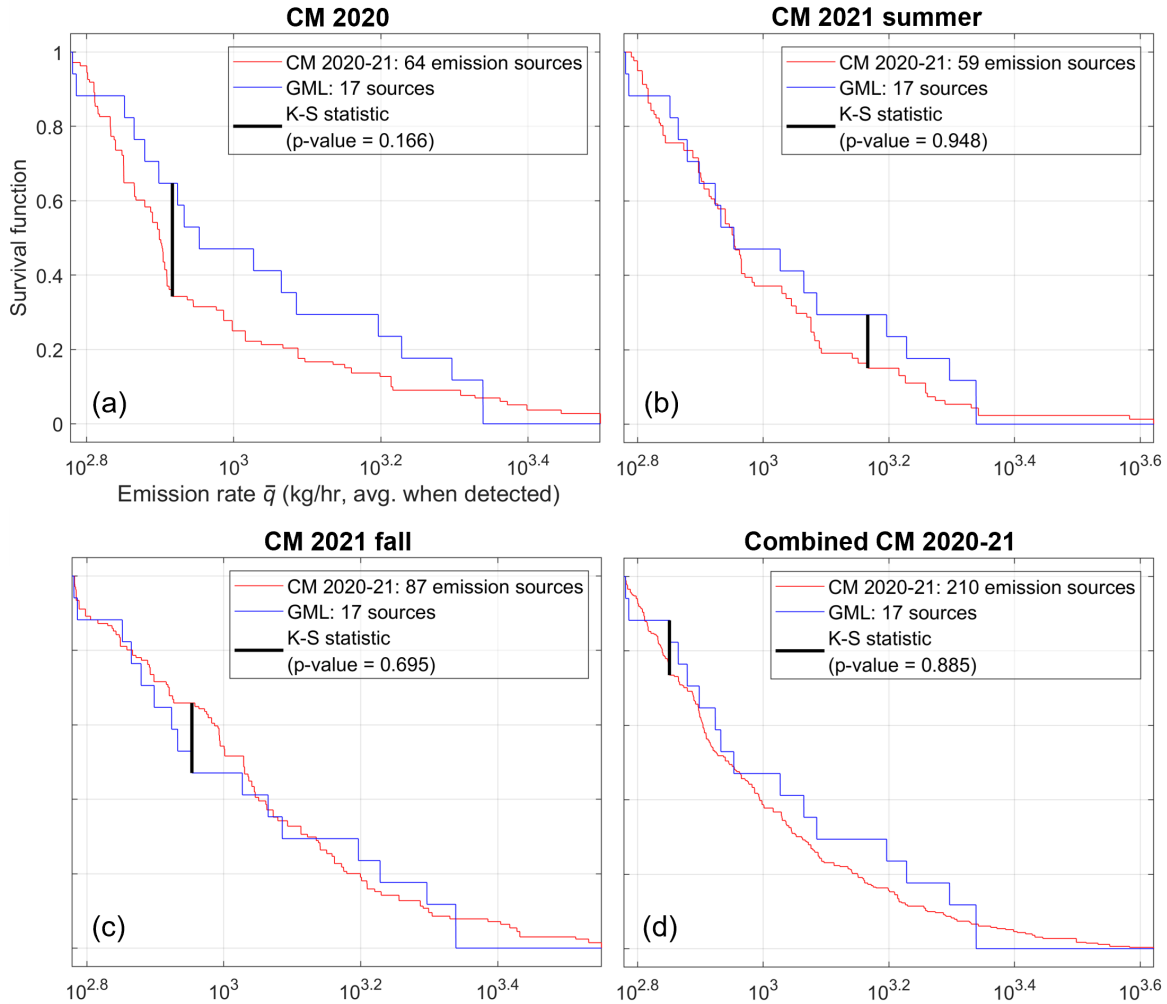


Figure S7: Survival function of CM 2020-21 and GML single-scan equivalent source detections (150 m aggregation diameter) for emission rates above  $600 \text{ kg h}^{-1}$  for campaigns taking place in (a) 2020 summer, (b) 2021 summer, (c) 2021 fall, and (d) all 2020-21 campaigns together. Kolmogorov-Smirnov (K-S) statistic and associated  $p$ -value for each case are indicated.

## 196 S4. Likelihood function

197 The likelihood function  $L(\theta)$ , where  $\theta$  is the vector of fit parameters, is based on the density  
 198 function from Eq. 1 normalized to the integration range  $x_{L,i} \leq x < \infty$ ,

$$p_i(x) = \frac{m}{bd_i\Gamma(1/m)} \exp\left(-\left|\frac{(x-x_0)}{b}\right|^m\right), \quad (\text{S5})$$

199 where  $x_{L,i}$  is the FDL,  $d_i = 1 - \text{sgn}(x_{L,i} - x_0)\Gamma[|(x_{L,i} - x_0)/b|^m, 1/m]$ , and the subscript  $i$   
 200 has been added to denote the sample (i.e. GML or CM). Using the standard form for the  
 201 likelihood function,  $L(\theta) = \prod_{j=1}^n p(X_j|\theta)$ , where  $X_j$  are the observed emission rates in the  
 202 sample, we obtain the log likelihood function for the  $i^{\text{th}}$  sample,

$$LL_i(\theta) = \sum_{j=1}^n \left[ \ln(f_{i,j}/\bar{f}_i) + \ln\left(\frac{m}{bd_i\Gamma(1/m)}\right) - \left|\frac{X_{i,j} - x_0}{b}\right|^m \right], \quad (\text{S6})$$

203 where  $\bar{f}_i$  is the mean persistence of the sample in the limited domain ( $x \geq x_{L,i}$ ). The term  
 204  $f_{i,j}/\bar{f}_i$  performs the persistence weighting (vertical part of the density transformation) from  
 205 persistence-adjusted to single-scan equivalent described in Sect. S2.4.1 while maintaining the  
 206 property that  $\int_{x_L}^{\infty} p(x)dx = 1$ .

207 For joint fits, because the samples are independent, we take the product of likelihoods to  
 208 obtain the joint log likelihood function

$$LL(\theta) = \sum_i LL_i(\theta), \quad (\text{S7})$$

209 where  $i = 1, 2$ .

## 210 S5. Akaike information criterion (AIC) analysis

211 AIC analysis was performed on lognormal and generalized lognormal fits to single-sample  
 212 data sets and joint data sets. Results are shown in Table S1. As seen by the location of

213 AIC minima under single-sample fits where the fit is tested with the same sample in the “1”  
 214 rows, joint fits do not provide the best representation of each single sample. They instead  
 215 reduce the joint likelihood of the two independent samples taken together, as seen by the  
 216 location of joint relative AIC minima under joint fit columns in “2” rows. Models fit to the  
 217 CM distribution alone tend to have very low values of joint relative likelihood of information  
 218 loss (see “3” rows), suggesting that models fit to the CM samples alone are not predictive  
 219 of the entire distribution through the range over which GML is assessed ( $\geq 3 \text{ kg h}^{-1}$  or  
 220  $\geq 10 \text{ kg h}^{-1}$ ). In addition to the lognormal and generalized lognormal functions shown, log-  
 221 logistic (with an extra parameter for horizontal shift) and power law model functions were  
 222 tested but were not optimal in any test case.

## 223 S6. Model fit and scaling

224 Results from the fit optimization for CM 2019 (150 m sources) are shown in Fig. S8. Measured  
 225 data in each survival function are plotted according to Eqn. S4, which scales each sample to  
 226  $S(x_{L,i}) = 1$  at the respective FDL,  $x_{L,i}$ , where  $i$  denotes the sample. The model function is  
 227 correspondingly normalized using integrals over the density  $p_i(x)$  given by Eqn. S5.

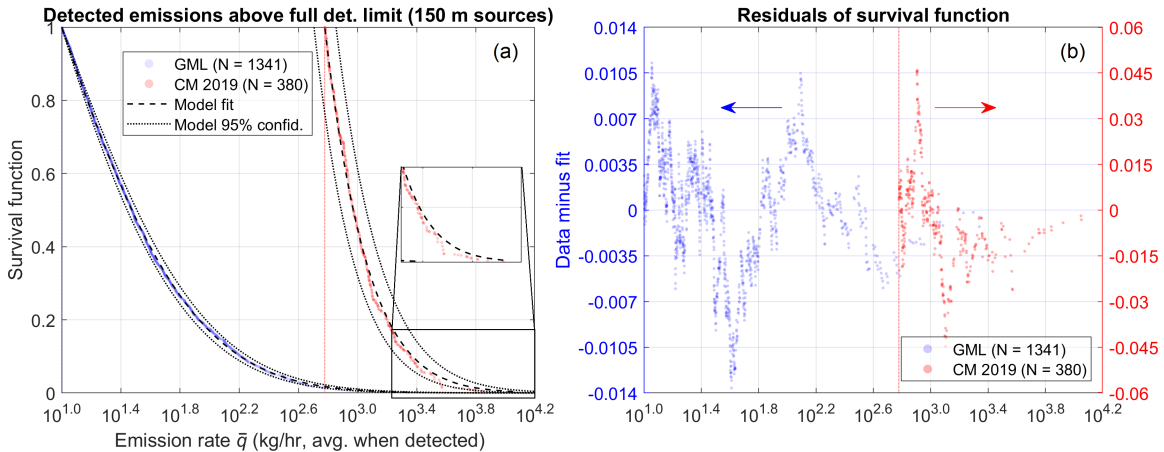


Figure S8: Joint model fitting of 150 m aggregated emission sources showing (a) survival function and (b) fit residuals. Inset: zoomed-in view of largest CM emission rates.

228 Residuals for both traces show that the survival function crosses the model multiple

Table S1: Akaike information criterion (AIC) analysis for different data sets: (a) CM 2019 survey data, 150 m emission sources; (b) CM 2019 survey data, single emitter (or equipment-sized) emission sources; (c) CM 2020-21 survey data, 150 m emission sources. Each table displays (1) AIC values obtained from the likelihood function (parameter values  $x_0, b, m$ ), (2) relative AIC values  $AIC_{rel,j} = AIC_{i,j} - AIC_{min,j}$ , where  $(i, j)$  signify (sample, fit), and (3) relative joint likelihood of information loss minimization, where the joint likelihood is taken as the product of likelihoods corresponding to each sample, i.e.  $\exp[-\sum_j AIC_{rel,j}/2]$ .

CM 2019, 150 m sources	(1)	<table border="1"> <thead> <tr> <th>Fit → ↓ Test</th> <th>CM Lognorm.</th> <th>GML Lognorm.</th> <th>Joint Lognorm.</th> <th>CM Gen.Logn.</th> <th>GML Gen.Logn.</th> <th>Joint Gen.Logn.</th> <th>Min.</th> </tr> </thead> <tbody> <tr> <td>CM</td> <td>54.0</td> <td>57.8</td> <td>55.4</td> <td>55.9</td> <td>75.8</td> <td>57.4</td> <td>54.0</td> </tr> <tr> <td>GML</td> <td>1873</td> <td>1080</td> <td>1081</td> <td>1112</td> <td>1081</td> <td>1083</td> <td>1080</td> </tr> <tr> <td>(Params)</td> <td>(1.840, 0.880)</td> <td>(0.880, 1.088)</td> <td>(0.797, 1.140)</td> <td>(-4.443, 6.057, 6.224)</td> <td>(-0.350, 2.167, 3.232)</td> <td>(0.882, 1.072, 1.929)</td> <td></td> </tr> </tbody> </table>	Fit → ↓ Test	CM Lognorm.	GML Lognorm.	Joint Lognorm.	CM Gen.Logn.	GML Gen.Logn.	Joint Gen.Logn.	Min.	CM	54.0	57.8	55.4	55.9	75.8	57.4	54.0	GML	1873	1080	1081	1112	1081	1083	1080	(Params)	(1.840, 0.880)	(0.880, 1.088)	(0.797, 1.140)	(-4.443, 6.057, 6.224)	(-0.350, 2.167, 3.232)	(0.882, 1.072, 1.929)	
	Fit → ↓ Test	CM Lognorm.	GML Lognorm.	Joint Lognorm.	CM Gen.Logn.	GML Gen.Logn.	Joint Gen.Logn.	Min.																										
	CM	54.0	57.8	55.4	55.9	75.8	57.4	54.0																										
	GML	1873	1080	1081	1112	1081	1083	1080																										
	(Params)	(1.840, 0.880)	(0.880, 1.088)	(0.797, 1.140)	(-4.443, 6.057, 6.224)	(-0.350, 2.167, 3.232)	(0.882, 1.072, 1.929)																											
	(2)	<table border="1"> <tbody> <tr> <td>CM</td> <td>0</td> <td>3.8</td> <td>1.4</td> <td>1.9</td> <td>21.9</td> <td>3.4</td> <td></td> </tr> <tr> <td>GML</td> <td>793</td> <td>0</td> <td>0.6</td> <td>32.0</td> <td>1.4</td> <td>2.6</td> <td></td> </tr> <tr> <td>Sum</td> <td>793</td> <td>3.8</td> <td>2.1</td> <td>33.9</td> <td>23.3</td> <td>6.0</td> <td>2.1</td> </tr> </tbody> </table>	CM	0	3.8	1.4	1.9	21.9	3.4		GML	793	0	0.6	32.0	1.4	2.6		Sum	793	3.8	2.1	33.9	23.3	6.0	2.1								
	CM	0	3.8	1.4	1.9	21.9	3.4																											
	GML	793	0	0.6	32.0	1.4	2.6																											
	Sum	793	3.8	2.1	33.9	23.3	6.0	2.1																										
	(3)	<table border="1"> <tbody> <tr> <td>0</td> <td>0.41</td> <td>1</td> <td>0</td> <td>0</td> <td>0.14</td> <td></td> </tr> </tbody> </table>	0	0.41	1	0	0	0.14																										
0	0.41	1	0	0	0.14																													
CM 2019, single emitter sources	(1)	<table border="1"> <thead> <tr> <th>Fit → ↓ Test</th> <th>CM Lognorm.</th> <th>GML Lognorm.</th> <th>Joint Lognorm.</th> <th>CM Gen.Logn.</th> <th>GML Gen.Logn.</th> <th>Joint Gen.Logn.</th> <th>Min.</th> </tr> </thead> <tbody> <tr> <td>CM</td> <td>-166</td> <td>-164</td> <td>-164</td> <td>-164</td> <td>-154</td> <td>-158</td> <td>-166</td> </tr> <tr> <td>GML</td> <td>67852</td> <td>3499</td> <td>3499</td> <td>6414</td> <td>3484</td> <td>3486</td> <td>3484</td> </tr> <tr> <td>(Params)</td> <td>(2.346, 0.541)</td> <td>(0.303, 1.056)</td> <td>(0.311, 1.052)</td> <td>(-6.901, 9.355, 16.52)</td> <td>(0.654, 0.731, 1.531)</td> <td>(0.629, 0.770, 1.619)</td> <td></td> </tr> </tbody> </table>	Fit → ↓ Test	CM Lognorm.	GML Lognorm.	Joint Lognorm.	CM Gen.Logn.	GML Gen.Logn.	Joint Gen.Logn.	Min.	CM	-166	-164	-164	-164	-154	-158	-166	GML	67852	3499	3499	6414	3484	3486	3484	(Params)	(2.346, 0.541)	(0.303, 1.056)	(0.311, 1.052)	(-6.901, 9.355, 16.52)	(0.654, 0.731, 1.531)	(0.629, 0.770, 1.619)	
	Fit → ↓ Test	CM Lognorm.	GML Lognorm.	Joint Lognorm.	CM Gen.Logn.	GML Gen.Logn.	Joint Gen.Logn.	Min.																										
	CM	-166	-164	-164	-164	-154	-158	-166																										
	GML	67852	3499	3499	6414	3484	3486	3484																										
	(Params)	(2.346, 0.541)	(0.303, 1.056)	(0.311, 1.052)	(-6.901, 9.355, 16.52)	(0.654, 0.731, 1.531)	(0.629, 0.770, 1.619)																											
	(2)	<table border="1"> <tbody> <tr> <td>CM</td> <td>0</td> <td>1.8</td> <td>1.7</td> <td>1.4</td> <td>12.1</td> <td>7.8</td> <td></td> </tr> <tr> <td>GML</td> <td>64336</td> <td>14.1</td> <td>14.2</td> <td>2930</td> <td>0</td> <td>1.8</td> <td></td> </tr> <tr> <td>Sum</td> <td>64336</td> <td>15.9</td> <td>15.9</td> <td>2931</td> <td>12.1</td> <td>9.7</td> <td>9.7</td> </tr> </tbody> </table>	CM	0	1.8	1.7	1.4	12.1	7.8		GML	64336	14.1	14.2	2930	0	1.8		Sum	64336	15.9	15.9	2931	12.1	9.7	9.7								
	CM	0	1.8	1.7	1.4	12.1	7.8																											
	GML	64336	14.1	14.2	2930	0	1.8																											
	Sum	64336	15.9	15.9	2931	12.1	9.7	9.7																										
	(3)	<table border="1"> <tbody> <tr> <td>0</td> <td>0.04</td> <td>0.04</td> <td>0</td> <td>0.30</td> <td>1</td> <td></td> </tr> </tbody> </table>	0	0.04	0.04	0	0.30	1																										
0	0.04	0.04	0	0.30	1																													
CM 2020-21, 150 m sources	(1)	<table border="1"> <thead> <tr> <th>Fit → ↓ Test</th> <th>CM Lognorm.</th> <th>GML Lognorm.</th> <th>Joint Lognorm.</th> <th>CM Gen.Logn.</th> <th>GML Gen.Logn.</th> <th>Joint Gen.Logn.</th> <th>Min.</th> </tr> </thead> <tbody> <tr> <td>CM</td> <td>-137</td> <td>-129</td> <td>-136</td> <td>-136</td> <td>-129</td> <td>-130</td> <td>-136</td> </tr> <tr> <td>GML</td> <td>14235</td> <td>1080</td> <td>1081</td> <td>1625</td> <td>1082</td> <td>1082</td> <td>1080</td> </tr> <tr> <td>(Params)</td> <td>(2.650, 0.500)</td> <td>(0.880, 1.088)</td> <td>(0.928, 1.059)</td> <td>(-4.713, 7.623, 17.04)</td> <td>(-0.350, 2.167, 3.232)</td> <td>(-1.957, 3.599, 4.494)</td> <td></td> </tr> </tbody> </table>	Fit → ↓ Test	CM Lognorm.	GML Lognorm.	Joint Lognorm.	CM Gen.Logn.	GML Gen.Logn.	Joint Gen.Logn.	Min.	CM	-137	-129	-136	-136	-129	-130	-136	GML	14235	1080	1081	1625	1082	1082	1080	(Params)	(2.650, 0.500)	(0.880, 1.088)	(0.928, 1.059)	(-4.713, 7.623, 17.04)	(-0.350, 2.167, 3.232)	(-1.957, 3.599, 4.494)	
	Fit → ↓ Test	CM Lognorm.	GML Lognorm.	Joint Lognorm.	CM Gen.Logn.	GML Gen.Logn.	Joint Gen.Logn.	Min.																										
	CM	-137	-129	-136	-136	-129	-130	-136																										
	GML	14235	1080	1081	1625	1082	1082	1080																										
	(Params)	(2.650, 0.500)	(0.880, 1.088)	(0.928, 1.059)	(-4.713, 7.623, 17.04)	(-0.350, 2.167, 3.232)	(-1.957, 3.599, 4.494)																											
	(2)	<table border="1"> <tbody> <tr> <td>CM</td> <td>0</td> <td>7.8</td> <td>7.1</td> <td>1.0</td> <td>7.8</td> <td>6.9</td> <td></td> </tr> <tr> <td>GML</td> <td>13155</td> <td>0</td> <td>0.2</td> <td>544</td> <td>1.4</td> <td>1.9</td> <td></td> </tr> <tr> <td>Sum</td> <td>13155</td> <td>7.8</td> <td>7.4</td> <td>545</td> <td>9.2</td> <td>8.7</td> <td>7.4</td> </tr> </tbody> </table>	CM	0	7.8	7.1	1.0	7.8	6.9		GML	13155	0	0.2	544	1.4	1.9		Sum	13155	7.8	7.4	545	9.2	8.7	7.4								
	CM	0	7.8	7.1	1.0	7.8	6.9																											
	GML	13155	0	0.2	544	1.4	1.9																											
	Sum	13155	7.8	7.4	545	9.2	8.7	7.4																										
	(3)	<table border="1"> <tbody> <tr> <td>0</td> <td>0.81</td> <td>1</td> <td>0</td> <td>0.39</td> <td>0.50</td> <td></td> </tr> </tbody> </table>	0	0.81	1	0	0.39	0.50																										
0	0.81	1	0	0.39	0.50																													

229 times without a strong bias toward the positive or negative values. However, CM residuals  
 230 are negative for emission rates above roughly  $10^{3.4}$  kg h<sup>-1</sup>. This does not strongly impact the  
 231 density function fit, but it does influence sample agreement with the model for cumulative  
 232 emissions (i.e. the integral of the density function, weighted by emission rate).

233 When plotted as density functions as in Fig. 2, traces are scaled to a common reference.  
 234 The factor  $1000/n_{\text{CM}}(x > x_{L,\text{CM}})$  is used to scale the CM data to 1000 detections above the  
 235 CM FDL, where  $n$  is the number of detected sources in the specified range. The GML series  
 236 is scaled by the factor

$$\frac{1000}{n_{\text{GML}}(x > x_{L,\text{GML}})} \frac{1}{\int_{x_{L,\text{CM}}}^{\infty} p_{\text{GML}}(x)}, \quad (\text{S8})$$

237 where “CM” or “GML” fill in the subscript  $i$  in Eqn. S5. The right-hand term of Eqn. S8  
 238 rescales the number of detected sources above the GML FDL by the ratio of the survival  
 239 functions to each FDL, where both terms in the ratio are evaluated at the CM FDL (that  
 240 is, recognizing the numerator as  $1 = \int_{x_{L,\text{CM}}}^{\infty} p_{\text{CM}}(x)$ ). These scale factors assume that the  
 241 size of both samples is sufficiently large above the respective FDL that sample error in the  
 242 number of detected sources is negligible. Likewise, the model function is scaled by the factor  
 243  $1000/\int_{x_{L,\text{CM}}}^{\infty} p_{\text{GML}}(x)$ , but with no assumptions about sample size.

244 Fit results in terms of the survival function are shown for CM 2019 equipment-scale  
 245 sources and CM 2020-21 150 m sources in Fig. S9. In cases where the CM residuals tend  
 246 to be negative but GML residuals tend to be positive, the fit is located in between the two  
 247 samples. To some extent, the model disagrees with CM due to the GML measurements in  
 248 these cases. Other possible reasons for the fit to be above the CM measurement distribution  
 249 in the heavy tail include (1) the model functional form or parameter values do not adequately  
 250 represent the rapid decline in sources in the fat tail, or (2) the heavy tails measured by CM  
 251 are reshaped relative to GML by other factors such as quantification bias, such as that  
 252 reported in Ref. 6. Assuming that the CM and GML measured distributions are in fact  
 253 aligned, apparent differences may be explained by the heavy tail of the distribution rolling  
 254 off faster than the model fits above emission rates of roughly  $10^{3.4}$  kg h<sup>-1</sup>.



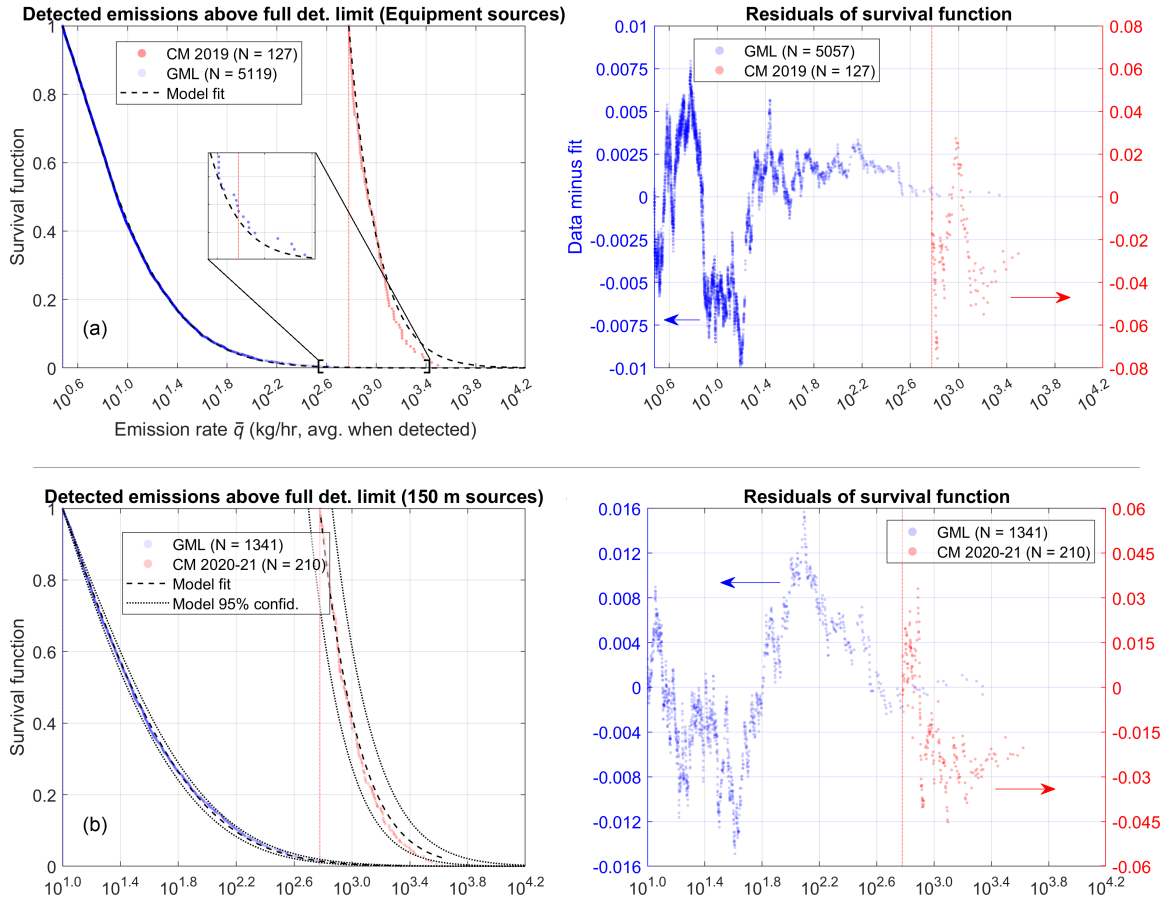


Figure S9: Survival function and residuals showing joint model fitting of GML to (a) CM 2019 equipment-scale sources and (b) CM 2020-21 facility-scale sources (150 m diameter). Inset (a): zoomed-in view of largest GML emission rates.

## 255 **S7. Equipment-scale emission source filtering**

256 Human analysts classified CM 2019 plume images as either “single emitter” or “multiple or  
257 unclear.” Detections classified as “single emitter” were selected for analysis. The data were  
258 cut to include only the first scan at each source, making the data set effectively single-scan  
259 ( $f = 1$ ). This filter changed the number of CM 2019 sources after other filters (pipelines,  
260 survey polygons) from 1348 at 150 m to 645 single emitters. For GML, skipping aggregation  
261 increased the number of GML sources from 2727 to 7176, though the number of GML sources  
262 above the CM FDL shrank from 17 to 9. Spatial aggregation significantly affects the CM  
263 distribution, whereas O&G pipeline sources do not (Section S11). Fit residuals display  
264 similar behavior to those from 150 m sources (Sect. S6).

## 265 **S8. Density plots (CM 2019 single emitters, CM 2020-21)**

266 Detected emission density from analysis with CM 2019 single emitter and CM 2020-21 sam-  
267 ples is shown in Fig. S10. As shown in Fig. S10a, the CM 2019 single emitter sensitivity  
268 at 50% POD is seen to be 321 [277, 382]  $\text{kg h}^{-1}$ . This overlaps with the confidence interval  
269 of the CM 2019 detection sensitivity at 150 m aggregation. Further details of the single  
270 emitter distribution in contrast to the 150 m distribution are described around Fig. 3. For  
271 the CM 2020-21 sample, Fig. S10b shows the density with CM 2019 traces reproduced for  
272 comparison. The sensitivity at 50% POD is 252 [227, 282]  $\text{kg h}^{-1}$ , which suggests a possible  
273 improvement over the CM 2019 sensitivity. The CM 2020-21 sample is scaled to the CM  
274 2019 sample using the ratio of the GML scale values given in Eqn. S8 from analysis with  
275 both CM samples, a value of 0.833. This ensures that the CM traces are scaled to one  
276 another such that the GML traces from both analyses coincide exactly. In other words, the  
277 CM traces are both scaled to 1000 total CM 2019 detections above the CM FDL using the  
278 GML distribution as a common reference.

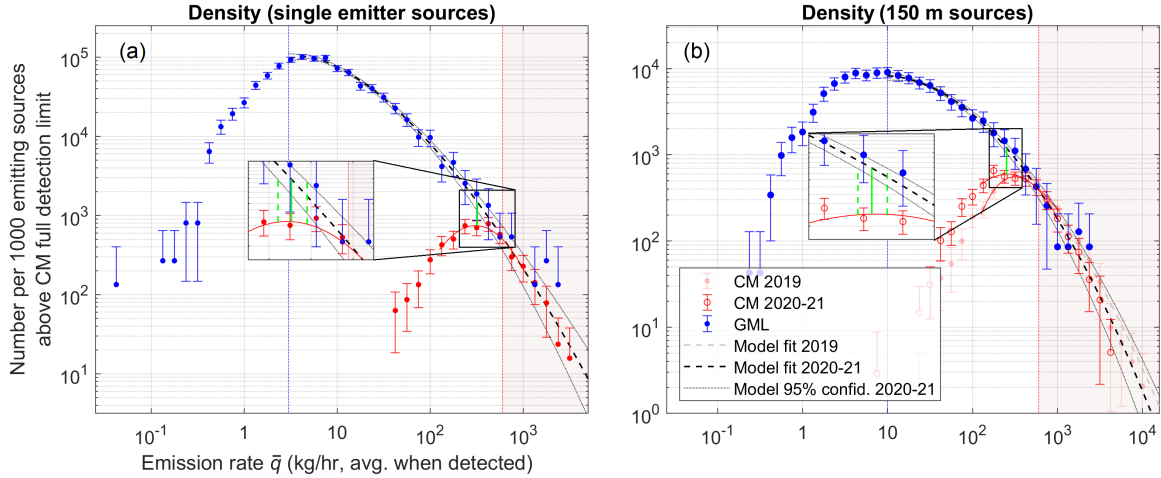


Figure S10: Emission source density from joint analysis with GML for (a) CM 2019 single emitters and (b) CM 2020-21 with 150 m sources. Zoomed in view near the CM sensitivity (insets) shows the 50% detection ratio with respect to model function and its confidence bounds.

## S9. Cumulative emission rate distribution (CM 2020-21)

The CM 2020-21 cumulative emission rate distribution is displayed in Fig. S11. CM 2019 measured data and model function are reproduced in the plot for comparison. Both CM data sets were analyzed jointly with the GML data set. By comparing the measured distributions at  $10 \text{ kg h}^{-1}$  to the model function and its confidence bounds at this emission rate, we find that CM 2020-21 measured 43.4% [37.8%, 49.2%] of the total cumulative emission rate from 150 m sources above  $10 \text{ kg h}^{-1}$ , whereas GML measured 98.2% [85.5%, 111.3%]. These results are similar to those obtained with CM 2019 data, suggesting consistency between the CM 2019 and 2020-21 campaigns.

Relative scaling of the CM 2020-21 density function to CM 2019 results in the different cumulative emission rate totals shown in the plot. This was performed as described in Sect. S8, where GML density was used as a reference. GML to CM scaling is implied directly from the joint fit without any ad hoc parameters. The ratio of measured totals between the two campaigns (CM 2020-21/CM 2019) is 91% when scaled to one another accounting for sample size and number of overflights, using GML as a reference.

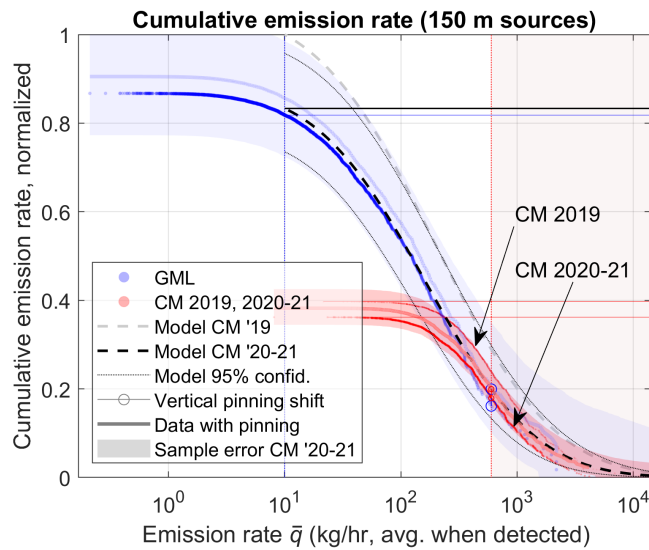


Figure S11: Cumulative emission rate distribution of GML and CM 2020-21 measurements with 150 m diameter aggregated emission sources. Joint GML/CM 2019 model and CM 2019 measured distribution are reproduced for comparison. Distributions from CM 2020-21 joint analysis are scaled to those from the CM 2019 analysis. All traces are normalized to equivalent campaign scale (spatial area, number of overflights). Vertically shifted copies of measured data pinned to the value of the model distribution at the CM FDL guide the eye, suggesting the shape of the measured distribution supposing sample error above the CM FDL were suppressed.

## 294 **S10. Monte Carlo estimation of sample error**

295 A Monte Carlo algorithm is used to obtain percentile ranges on the cumulative emission rate  
296 as a function of source emission rate. New samples are synthesized from the joint best-fit  
297 density function at emission rates above the respective FDL. Size of synthesized samples  
298 matches the number of detected sources above the FDL in the measured samples. Since  
299 the density function expresses the single-scan equivalent, the number of overflights is one  
300 for each synthesized detection. For each of  $n_{MC} = 10,000$  Monte Carlo trials, a vector of  
301  $n(x < x_{L,i})$  random numbers uniformly distributed on the interval  $(0, 1)$  is generated. The  
302 random numbers are input as arguments to the inverse of the survival function on the domain  
303 above the FDL to generate source emission rates. Cumulative emission rate versus source  
304 emission rate is calculated from each Monte Carlo trial. Percentiles are found from the set  
305 of synthesized Monte Carlo trials on a grid of source emission rates.

306 Simulated sample error supports the emission rate domain down to each respective FDL.  
307 Sample error below the FDL is represented by assuming the same cumulative emission rate  
308 increase as the measured sample, with no additional error contributed by samples below the  
309 FDL.

## 310 **S11. Exclusion of pipelines from CM data set**

311 Exclusion of O&G pipeline sources in the CM 2019 sample produces negligible change in the  
312 survival function. By comparison, the effect of filtering the data to single emitter sources  
313 changes the distribution significantly. Fig. S12 shows the survival function for “with pipeline”  
314 and “without pipeline” data sets for 150 m and single emitter aggregation styles. Moderate  
315  $p$ -values, and hence no statistically significant difference, are seen between the distributions  
316 including or excluding pipelines within each aggregation style. However, the  $p$ -value for  
317 a comparison across aggregation styles is outside the 95% confidence interval ( $p < 0.05$ ),  
318 indicating that those distributions differ significantly.

319 Despite the lack of significant change in the shape of the CM 2019 distribution with the  
 320 inclusion or exclusion of pipelines, small differences around the detection roll-off ( $300 \text{ kg h}^{-1}$ )  
 321 lead to slightly different estimates of the detection sensitivity. Density functions for both  
 322 aggregation styles with and without pipelines are shown in Fig. S13. Comparing the model  
 323 bounds at 95% confidence to respective cubic polynomial roll-off fits yields detection sen-  
 324 sitivity intervals of 233-279 (with pipelines) and 256-309  $\text{kg h}^{-1}$  (no pipelines) for 150 m  
 325 sources, and 258-356 and 277-382  $\text{kg h}^{-1}$ , respectively, for single emitter sources. Since these  
 326 intervals overlap significantly, the detection sensitivity roll-off can be considered as weakly  
 327 dependent on both types of data filter.

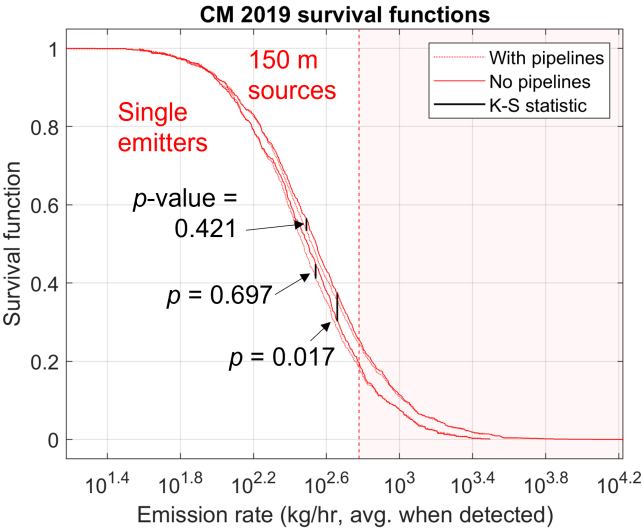


Figure S12: Comparison of CM 2019 survival functions over the range of emission rates in the sample. Data are filtered to either include or exclude O&G pipeline emission sources at both 150 m aggregation and single emitter sources.  $p$ -values are indicated for “with pipeline” and “without pipeline” comparisons within each source type and a “no pipeline” comparison across the two source types.

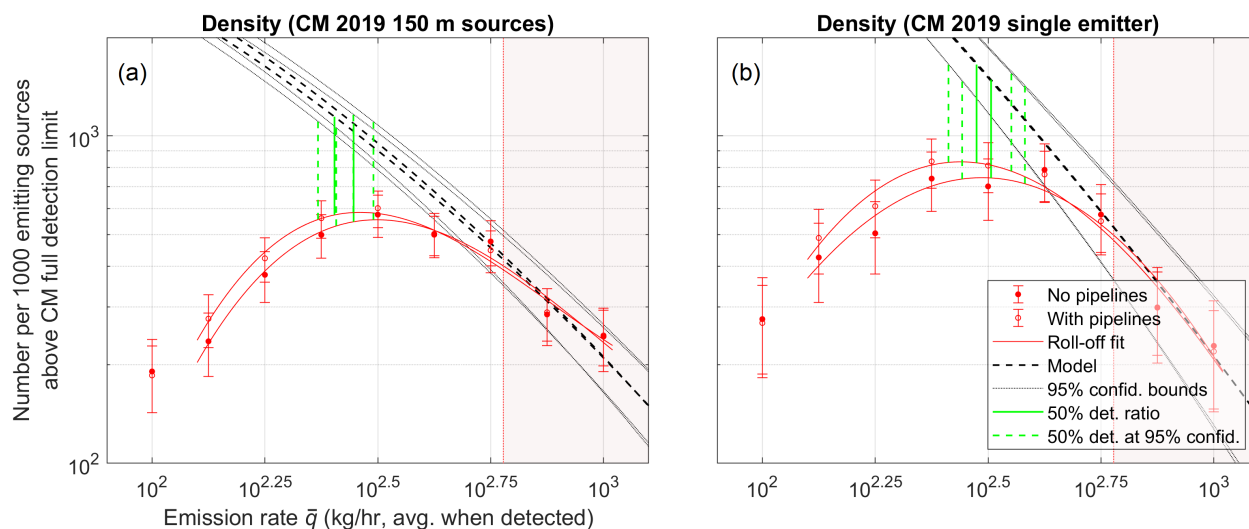


Figure S13: CM 2019 detected emission density plots showing influence of O&G pipeline sources on emission distribution around detection roll-off. 150 m aggregated sources (a) and single emitter sources (b). Model functions are reproduced from joint analysis with GML.

## References

- (1) Cusworth, D. H.; Duren, R. M.; Thorpe, A. K.; Olson-Duvall, W.; Heckler, J.; Chapman, J. W.; Eastwood, M. L.; Helmlinger, M. C.; Green, R. O.; Asner, G. P.; Dennison, P. E.; Miller, C. E. Intermittency of Large Methane Emitters in the Permian Basin. *Environmental Science and Technology Letters* **2021**, *8*, 567–573.
- (2) Cusworth, D. Methane plumes for NASA/JPL/UArizona/ASU Sep-Nov 2019 Permian campaign. 2021; [Data set]. Zenodo. <https://doi.org/10.5281/zenodo.5610307>.
- (3) Cusworth, D. Methane plumes from airborne surveys. 2021; [Data set]. Zenodo. <https://zenodo.org/record/7072824#.ZELKvM7MKUu>.
- (4) Cusworth, D. H.; Thorpe, A. K.; Ayasse, A. K.; Stepp, D.; Heckler, J.; Asner, G. P.; Miller, C. E.; Yadav, V.; Chapman, J. W.; Eastwood, M. L.; Green, R. O.; Hmiel, B.; Lyon, D. R.; Duren, R. M. Strong methane point sources contribute a disproportionate fraction of total emissions across multiple basins in the United States. *Proceedings of the National Academy of Sciences* **2022**, *119*, e2202338119.

- 342 (5) Bartoszyński, R.; Niewiadowska-Bugaj, M. *Probability and Statistical Inference*; Wiley,  
343 1996; Chapter 16.
- 344 (6) Rutherford, J. S.; Sherwin, E. D.; Chen, Y.; Aminfard, S.; Brandt, A. R. Evaluating  
345 methane emission quantification performance and uncertainty of aerial technologies via  
346 high-volume single-blind controlled releases. preprint at [https://doi.org/10.31223/  
347 X5KQ0X](https://doi.org/10.31223/X5KQ0X).